Ligand-Mediated Endocytosis Is Regulated in A Sexually Dimorphic Way in Osteocytes *in vivo*

Melia Matthews[1], Alexander Saffari[1], Nuzhat Mukul[1], Joyce Hai[1], Nada Naguib[1], Ulirich B. Wiesner[2,3], and Karl J. Lewis[1,✉]

[1]Department of Biomedical Engineering, Cornell University, 237 Tower Rd, Ithaca,14850, New York, USA
[2]Department of Materials Science and Engineering, Cornell University, Bard Hall 210, Ithaca, 14850, New York, USA
[3]Kavli Institute at Cornell for Nanoscale Science, Cornell University, Ithaca 14853, New York, USA

Abstract

Endocytosis is an important ubiquitous cellular function, particularly for mechanically responsive cells. Recent advancements in intravital imaging have made it possible to study basic functions of bone cells *in vivo*. Here, we report intravital investigation of endocytosis in osteocytes, the resident bone mechanosensor. We combined multiphoton microscopy with surgical exposure of the third metatarsal to achieve real-time imaging of intracellular fluorescent nanoparticle dynamics in osteocytes *in vivo*. We paired this novel approach with pharmacological perturbation of broad endocytic pathways to interrogate differences between non-specific and receptor mediated endocytosis. Our findings indicate extremely fast endocytic activity in osteocytes, with evidence of successful targeting of integrins for ligand-mediated uptake. Moreover, we found that dynamin-dependent endocytosis is regulated in a sexually dimorphic manner in osteocytes. Using our novel platform, we report the first *in vivo* data of endocytic activity in bone cells, and the first general evidence of direct chemical perturbation of ligand-mediated endocytosis *in vivo*.

osteocyte | fluorescent nanoparticles | integrin | endocytosis
Correspondence: *kjl235@cornell.edu*

1. Introduction

Osteocytes, the resident mechanosensors of bone, orchestrate the activity of bone resorbing osteoclasts and bone depositing osteoblasts to achieve a functionally healthy skeleton (1–3). Their unique 3D microenvironment in bone tissue is critical for mechanotransduction responses to tissue-level deformation (4). Transmembrane integrin proteins are a vital feature of osteocyte interactions with their extracellular matrix. They create punctate connections between the osteocyte process cell membrane and bone matrix that function as sites of fluid flow mechanical activation (5, 6). Despite the evident importance of membrane bound components in osteocytes (7), little is known about how these and other mechanoactive surface features are maintained, particularly *in vivo* (8–10). Clues from other tissues point to maintenance via complex endocytosis and membrane cycling mechanisms (11–13). Endocytosis is when extracellular objects (e.g., ligands, surface proteins, channels, nanoparticles) are engulfed in the plasma membrane and internalized as an endosome to the cytosol. It is involved in maintenance of membrane bound channels (14), receptors (15, 16), reuptake of neurotransmitters (17–19), and regulation of mechanotransduction machinery (13, 20). Although the literature on endocytosis in osteocytes is limited, essential findings have been reported for bone generally. Conditional deletion of caveolin-1 in mouse osteoblasts leads to increased bone formation rate, bone volume, and improved tissue mechanical properties of the bone compared to controls (21, 22). These results suggest a meaningful role for caveolin endocytosis in the mechanical adaption of bone. Endosomal regulation of important bone cytokines like parathyroid hormone and transforming growth factor-β have been reported in osteoblasts (23, 24). Wnt and Notch signaling pathways are also mediated by endocytosis of transmembrane proteins (25, 26), though this has not been studied explicitly in bone cells.

Much of what we know about endocytosis comes from work in yeast (27, 28), fruit flies (29), and mammalian cell culture experiments (30–33). Several pharmacology-based interventions have been used to modulate endocytosis *in vitro*. Dyngo4a is a potent dynamin inhibitor derived from Dynasore that blocks dynamin G domain GTPase activity and perturbs receptor-mediated endocytic pathways (34). Disruption of clathrin-mediated pathways by small molecule drugs like Dyngo4a can abrogate receptor uptake in adenocarcinoma cells, fibroblasts, and neurons *in vitro* (34, 35). Internalization pathways independent of clathrin have also been observed in protein trafficking, notably cholesterol-mediated endocytosis (36–38) and micropinocytosis (39). Methyl-β-cyclodextrin (MβCD) is a cholesterol and lipid raft depleting agent that is known to disturb cholesterol-mediated endocytosis in numerous cell types (40–43).

Investigation of endocytosis in osteocytes remains limited because visualizing subcellular activities in osteocytes *in situ* is technically challenging. Multiphoton microscopy offers improved spatial and temporal resolution *in vivo* and has facilitated a recent push to study endocytosis in intravital tissues (44). Research in this field has focused on a few model organ systems such as the kidneys and the salivary glands and has primarily utilized fluorescently labeled dextran as their exogenous marker for bulk endocytosis (45–47). Viewing and quantifying cellular dynamics *in vivo* allows researchers to bypass *in vitro* limitations concerning tissue dynamics and endocrine signaling and to focus efforts on the most physiologically relevant models that are currently available.

Our group is at the leading edge of establishing intravital imaging approaches generally and in bone tissue specifically using two-photon microscopy. To the best of our knowledge, no research has been performed on the role of endocytosis in bone or other musculoskeletal tissues *in vivo*. Recently, we reported a novel intravital imaging approach for studying cellular activity in a fully functioning, systemically attached long bone (48, 49). This platform can be used to interrogate endocytosis mechanisms in musculoskeletal tissue *in vivo* while keeping the unique 3D microenvironment and key endocrine factors intact. A local, subcutaneous injection of ultrasmall and bright fluorescent core-shell silica nanoparticles synthesized in water (C'Dots, diameter $\leq$ 7 nm) to the mouse third metatarsal (MT3) provides swift and robust fluorescence signal in cortical bone osteocytes *in vivo* (49). C'Dots display rapid cellular internalization and clearance and can be functionalized to target distinct uptake mechanisms. We aimed to use this intravital imaging platform to establish a baseline understanding of osteocyte nanoparticle endocytosis *in vivo*.

Here, we use untargeted, transmembrane integrin-targeted, and cell membrane penetrating nanoparticles to visualize a broad range of endocytic pathways in osteocytes in real-time (Figure 1). We combined these three C'Dot types with the broadly acting small-molecule endocytosis disruptors Dyngo4 and MβCD to modulate potential innate osteocyte uptake and trafficking mechanisms. We hypothesize that discrete endocytic pathways control the uptake of targeted, untargeted, and cell membrane penetrating nanoparticles in osteocytes *in vivo*. We assess how a local injection of these broad-acting drugs impacts osteocyte metabolism and clearance of C'Dots *in vivo* at both acute and extended time points.

2. Methods

2.1 Animals: Male and female skeletally mature young adult C57Bl/6J mice (16-20 weeks old) were used for all nanoparticle uptake and clearance experiments (Jackson Laboratory, Bar Harbor, ME). Intracellular co-localization experiments utilized an established mouse line with osteocyte-targeted expression of the genetically encoded calcium indicator (GECI) GCaMP6f (50). These mice were bred in house by crossing Ai95-D mice [B6J.Cg-Gt(ROSA)26Sortm95.1(CAG-GCaMP6f)Hze/MwarJ; JAX Labs] with DMP1/Cre mice [B6N.FVB-Tg(Dmp1-cre)1Jqfe/BwdJ; JAX Labs], which have Cre recombinase driven by the DMP1 promoter, a gene predominantly expressed in osteocytes (51). All procedures were approved by the Institutional Animal Care and Use Committees of Cornell University.

2.2 Synthesis of ultrasmall PEGylated, cRGD, and TAT functionalized Core-Shell Silica Nanoparticles: Ultrasmall fluorescent core-shell silica nanoparticles (C'Dots) with covalently encapsulated Cy5 dye (from Cy5-maleimide (Lumiprobe) with net positive charge conjugated to (3-mercaptopropyl)trimethoxysilane (MPTMS; Sigma-Aldrich) in a silica core (from TMOS; Sigma-Aldrich) and poly(ethylene glycol) (PEG) shell (from methoxy-PEG(6-9)-silane (500 g/mol); Gelest) were synthesized in water as previously described (52, 53). Three varieties of C'Dots were synthesized: 1) Untargeted control C'Dots (PEG-Cy5-C'Dots) - subsequently referred to as PEG-C'Dots. 2) Integrin targeting C'Dots surface functionalized with integrin-targeting cyclic(arginine-glycine-aspartic acid-D, tyrosine-cysteine) peptide, (c(RGDyC)-PEG-Cy5-C'Dots) - subsequently referred to as RGD-C'Dots. RGD-C'Dots were functionalized by adding cRGDyC-PEG-silane to the particle core in the PEGylation step as described in detail elsewhere (52, 54). 3) C'Dots capable of penetrating membranes, including endosomal escape, were surface functionalized with human immunodeficiency virus (HIV) TAT peptides (TAT-PEG-Cy5-C'Dots) - subsequently referred to as TAT-C'Dots. TAT-C'Dots were prepared similar to previously reported methods (55), but using an improved click chemistry approach. The TAT peptide sequence used was 5-azido-pentanoyl – RKKRRQRRR-NH2 (Biosynth). The terminal azido group of the peptide was clicked onto the C'Dot surface functionalized with dibenzocyclooctyne (DBCO) via azide-alkyne cycloaddition. The DBCO functionalized C'Dots were prepared using post-PEGylation surface modification by insertion (PPSMI) method as described in detail elsewhere (56). To that end, small functional aminopropyl-trimethoxy-silane (APTMS) was first inserted between PEGs on the silica surface. Resulting NH2-C' dots were then reacted with DBCO-PEG4-N-hydroxysuccinimidyl ester (DBCO-PEG4-NHS ester, Santa Cruz Biotechnology) yielding DBCO-C'Dots. From particle characterization efforts employing a combination of fluorescence correlation spectroscopy (FCS) and UV-Vis absorbance data, with methods described elsewhere (56), PEG-, RGD-, and TAT-C'Dots exhibited hydrodynamic radii of 5.7, 5.5, and 6.0nm, respectively, and number of dyes per C'Dot of 2.0, 2.1, and 2.0, respectively (Supp. Fig. S1). Furthermore, RGD-C'Dots were estimated to have 20 cRGDyC ligands per particle and TAT-C'Dots were estimated to have 10 TAT (5-azido-pentanoyl – RKKRRQRRR-NH2) peptides per particle.

2.3 Endocytosis Modulating Drugs: The small molecule Dyngo4a (Abcam) was used as a potent Dynasore analog to evaluate the impact of dynamin-mediated endocytosis inhibition on osteocyte C'Dot uptake and metabolism *in vivo*. The molecule disrupts dynamin GTPase activity and its role in pinching off budding endocytic vesicles (34). Dyngo4a was diluted from a stock solution in DMSO to the working concentration of 30μM in 1x DPBS. Dyngo4a working solution was kept at -20°C and was brought to room temperature before use. Water-soluble oligosaccharide methyl-β-cyclodextrin (MβCD, Sigma) binds to and removes cholesterol from the plasma membrane and is used to evaluate the impact of cholesterol-mediated lipid raft-based endocytosis inhibition (42). MβCD was diluted from a powder to its working concentration of 10mM in 1x DPBS. MβCD was kept at 4°C and brought to room temperature before use.

2.4 Drug Injection and Incubation: Mice were anesthetized with 2-3% isoflurane mixed with medical grade air in an induction chamber for 3 minutes before injection. Restraint of

the mice was necessary to maintain reliable reproduction of the precise injection procedure. During injection, mice were kept under 2% isoflurane with a nose cone. A 10μL bolus was subcutaneously injected above the MT3 30 minutes before C'Dot injection and subsequent imaging. A local injection was used to minimize the off-target endocrine effects of a systemic injection. A 10μL control bolus of 1x DPBS was used on control groups in the acute clearance study. No control bolus was used in the extended clearance study. Mice were allowed normal cage activity during the 30-minute drug pre-incubation time.

2.5 C'Dot Injection and Incubation: After drug or control bolus preincubation, mice were re-anesthetized for nanoparticle injection. A 10μL subcutaneous injection of 10μM PEG-, RGD-, or TAT-C'Dots was then administered over the third metatarsal (MT3). For the acute clearance study, C'Dots were incubated for 5 minutes and mice were kept under nose cone anesthesia before MT3 isolation and imaging (n=4-5/group/sex). For the extended clearance study, C'Dots were incubated for 45 minutes before MT3 isolation. Mice were allowed normal cage activity during the 45-minute incubation and were re-anesthetized immediately before MT3 isolation surgery (n=3-5/group/sex).

2.6 Metatarsal Isolation Surgery: MT3 bones were isolated as previously described (48, 49). Briefly, while mice were anesthetized, a shallow incision was made between the second and third metatarsal on the dorsal aspect of the mouse hind paw, and overlying tendons were removed. The MT3 was then functionally isolated from the rest of the paw with a stainless steel pin beneath the mid-diaphysis of the bone, leaving primary vasculature at the proximal and distal palmar aspects intact. The bone was secured in a 3-point bending configuration and submerged in room temperature 1xDPBS. Mice were continuously anesthetized with a nose cone at 1.5-2% isoflurane during all subsequent imaging.

2.7 Imaging: Fluorescent signal inside the functionally isolated MT3 was visualized with multiphoton microscopy (MPM) (Bergamo II, Thorlabs) as previously described (49). Briefly, a 20x immersion objective (XLUMPLFLN, Olympus), 1090nm wavelength excitation, and a >647 nm long pass filter acquisition were used for observation of Cy5 encapsulated C'Dots. Images were captured at 1024x1024 pixel density and 0.588μm pixel resolution. A 35μm z-stack was taken for each mouse, starting 20μm beneath the bone surface, with 0.3μm steps between each slice and averaging of 7 frames per slice. In the acute clearance study, after the 5-minute incubation, imaging occurred every 3 minutes for 30 minutes for a total of 10 stacks. During the extended clearance study, after the initial 45-minute incubation, imaging occurred every 15 minutes over a period of 2.5 hours, also resulting in ten stacks (experimental timelines for the acute and extended imaging studies are depicted in Figure 1. Timelapse videos use the same pixel density and resolution, capturing an image every 30 seconds for 15 minutes. Co-localization imaging experiments with GCaMP6f mice used a second volumetric z-stack with an excitation of 920nm and 525 ± 25nm bandpass filter acquisition to collect intracellular calcium signal. Experiments looking at C'Dot dendritic signal used a 5-minute C'Dot incubation before MT3 isolation. Averaging was increased to 20 frames per slice to visualize the fine structure of osteocyte dendrites.

Images showing colocalization of C'Dots and third harmonic generation (THG) signal were collected using a 3-photon system created in the Xu and Schaffer Labs at Cornell (57). Briefly, an Opera-F amplifier laser (Coherent) with an excitation of 1680nm and a 25x water-immersion objective (XLPLN25XWMP, Olympus) was used. The mouse hind paw with functionally isolated MT3 bone (as described above) was immersed in heavy water (D2O) to reduce absorption of the excitation laser. THG signal was detected through a 558 ± 10nm bandpass filter (Semrock) by an ultra bialkali PMT (R7600-200, QE at 560 nm, 10%, Hamamatsu Photonics) while red Cy-5 C'Dot signal was detected through a 593nm long-pass filter (Semrock). A 35μm z-stack was obtained with 0.3μm steps between each frame. MATLAB (MathWorks) software running the ScanImage (58) module mediated image collection.

2.8 Image Analysis: Z-stacks for all imaging sessions of each mouse were analyzed in ImageJ (NIH) as previously described (49). Briefly, a macro was created to filter the images and to interpolate the cortical bone regions of interest across the z-stack depth. Then 3D segmentation created objects for all cell volumes over a threshold signal intensity. The threshold value was established as the mean grey value of background region of interest (ROI) plus 3x standard deviation. Segmented objects were then filtered by surface area (>1000 pixels) to ensure only full cell volumes were counted. The total number of objects with C'Dot signal was collected for each imaging time point. The mean intensity for each object was also quantified using the 3D Manager tool. Intensities were normalized to the background within each z-stack.

2.9 Quantification of C'Dot Subcellular Localization: The first frame from each z-stack taken after C'Dot incubations was analyzed for subcellular localization within osteocytes. PEG- and RGD-C'Dot groups were quantified under the following study conditions of: no drug, Dyno4a pre-incubation, and MβCD pre-incubation. Images were filtered with a Gaussian blur, thresholded, and cellular ROIs containing C'Dot signal were identified with the "Analyze Particle" tool. These ROIs were overlayed onto the original un-blurred image to assist with cell visualization. Cells were binned as having either distinct subcellular localization of C'Dots or saturated/non-distinct signal. The number of cells with subcellular localization was reported as a percentage of total cells in each frame.

2.10 Statistical Analyses: Clearance study analysis was performed using 2-way ANOVAs and regressions, including non-linear (one-phase decay) and linear regressions. Quantification of changes between acute and extended clearance studies used a student's T-Test on the final acute time point and the initial extended time point. Subcellular localization analysis used student's T-Tests between drug groups within sex and C'Dot type. Analyses were performed in GraphPad Prism version 9.0 for Mac OS X (GraphPad Software).

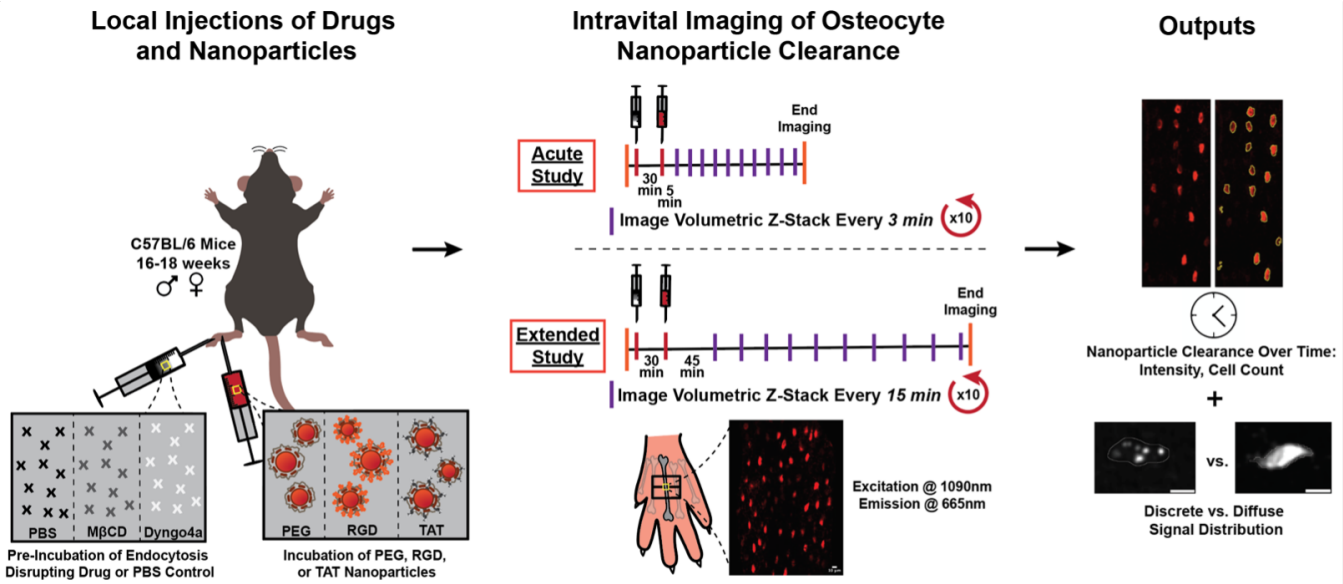

Fig. 1. Graphical abstract of experimental design for imaging intravital C'Dot uptake and clearance in bone. Both endocytosis disrupting drugs and fluorescent nanoparticles were exposed to bone and osteocytes through a local subcutaneous injection above the third metatarsal (3MT) bone in a mouse hind paw. After a 30-minute pre-incubation of the drugs or control, C'Dot nanoparticles were injected and incubated before surgical MT3 isolation and imaging of cortical bone osteocytes. The acute experiment had a 5 min C'Dot incubation time and z-stack images were taken every 3 minutes for 30 minutes. The extended experiment utilized a 45-minute C'Dot incubation time and z-stack images were taken every 15 minutes for 2.5 hours. Images from both experiments were analyzed for clearance kinetics of nanoparticle signal as well as subcellular distribution of signal. Scale bars = 10μm.

A mixed model on extended clearance data was also run in RStudio version 2023.12.1+402 using the lme4 package.

2.11 Overall Study Design: Osteocytes in C57Bl/6J mouse third metatarsals were exposed to Dyngo4a and MβCD small molecule drugs via a local subcutaneous injection. These drugs were assessed for their ability to modulate osteocyte uptake, metabolism, and trafficking of locally delivered nanoparticles. Previously validated fluorescent nanoparticles (C'Dots) were used to observe changes in osteocyte activity *in vivo* (49). Either untargeted PEG-C'Dots, integrin-targeting RGD-C'Dots, or membrane-penetrating/endosomal escaping TAT-C'Dots were injected into the mouse hind paw 30 minutes after preincubation with Dyngo4a, MβCD, or a control PBS bolus (Figure 1). Three C'Dots types with distinct cellular uptake pathways and two broadly acting drugs were used to establish a better fundamental understanding of osteocyte nanoparticle endocytosis *in vivo*. Volumetric multi-photon near-infrared imaging of C'Dot signal over time was used to quantify drug induced changes in osteocyte C'Dot uptake and retention. Both Dyngo4a and MβCD were tested across all groups: male and female, PEG-, RGD-, and TAT-C'Dots for both acute and extended clearance studies (n=4-5/group/sex).

3. Results

3.1 C'Dot Co-localization with Osteocytes *in vivo* Initial assessment of nanoparticle endocytosis requires confirmation that the particles have been taken up into the cells and are not merely attached to the cell membrane. We previously reported co-localization of C'Dots with calcein-AM in cortical bone osteocytes *in vivo* (49). Here we add two additional co-localization metrics. First, a genetically modified mouse strain with GCaMP6f calcium signal (50) expressed under the DMP-1 promoter was utilized. All living osteocytes in these mice with physiologically relevant calcium levels have cytosolic green fluorescent signal (48). Local subcutaneous injections of C'Dots incubated for 45 minutes resulted in high levels of signal overlap between the red Cy5 signal and the green calcium signal (Figure 2). An untargeted PEG-C'Dot injection generated 78% of cells with complete C'Dot signal overlap. An injection of integrin-targeted RGD-C'Dots created a slightly increased level of cellular overlap at 83%. These results strongly support that fluorescent C'Dot signal is predominantly interior to the osteocyte cell membrane rather than in the extracellular space. In another set of data, we used 3-photon microscopy and endogenous THG signal to compare C'Dot localization to material interfaces, such as those between the bone matrix and the fluid filled osteocyte lacunae. Injected C'Dot signal was found to localize within peaks of THG signal, indicating that a majority of C'Dots do not remain in the extracellular fluid or attach to the bone mineral matrix, but are instead internal to the cell (Figure 2). Together these data support the internalization of C'Dots by osteocytes following our subcutaneous injection, suggesting an endocytic mechanism of nanoparticle uptake.

3.2 Acute Osteocyte C'Dot Uptake and Clearance with Endocytic Inhibitors. To test acute uptake and clearance dynamics of C'Dots in osteocytes *in vivo*, we preincubated MT3s with endocytic inhibitors MβCD and Dyngo4a. Representative images from each group during the first acute imaging timepoint clearly show a qualitative impact of the

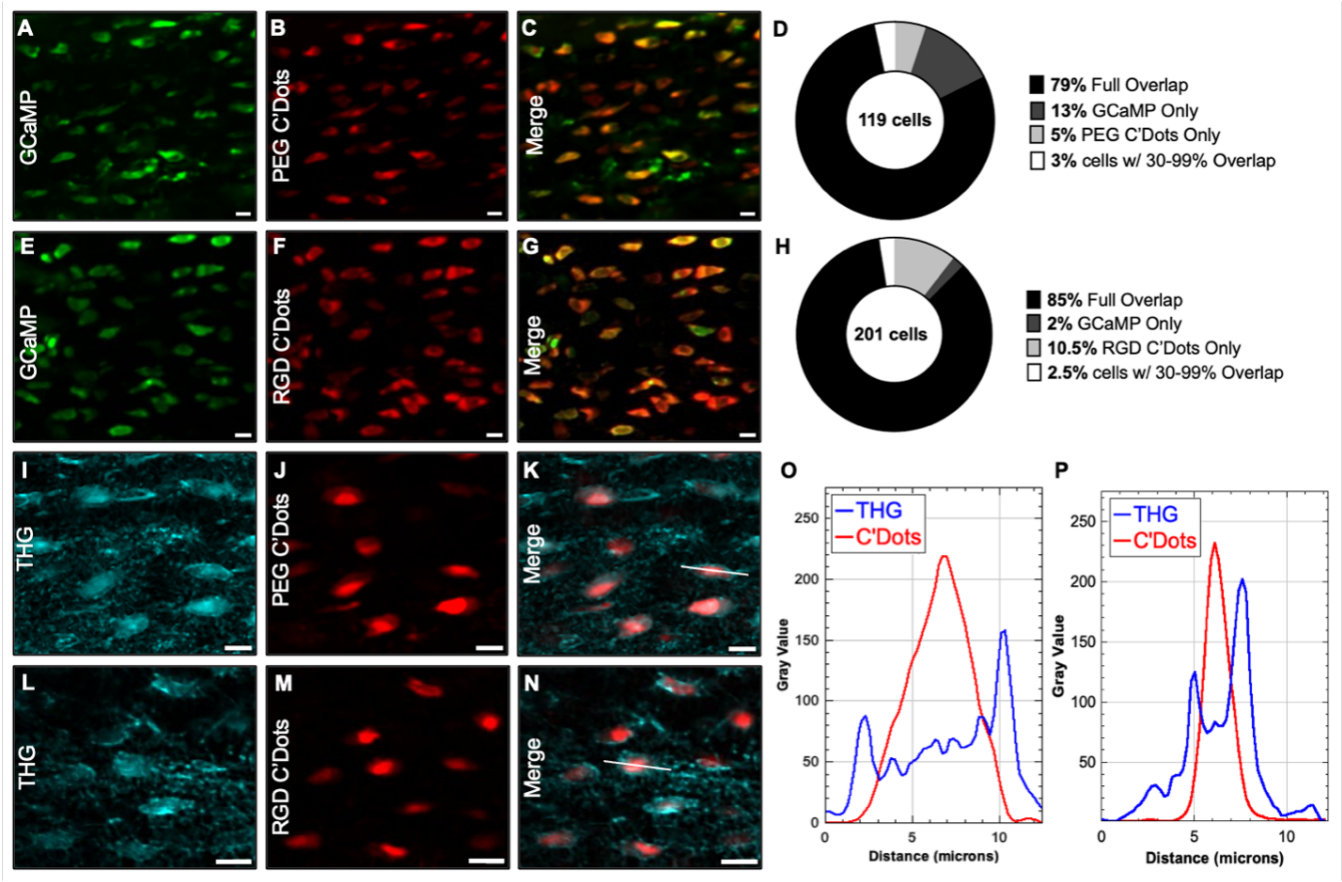

Fig. 2. Co-localization of C'Dot signal in osteocytes in vivo. To confirm the cellular uptake of the C'Dot nanoparticles, we performed distinct co-localization experiments with both 2-photon and 3-Photon microscopy. In the 2-Photon experiments, genetically modified mice expressing GCaMP6f signal within osteocytes were locally injected with PEG (A-C) and RGD (E-G) C'Dots for a 45-minute incubation before imaging. GCaMP signal (green) was collected at 920nm excitation and C'Dot signal (red) was collected at 1090nm excitation. Co-localization analysis on the overlap of signal showed a high percentage of cells with full or partial overlap for both PEG (D) and RGD (H) C'Dots. For the 3-Photon experiment, wild-type mice were locally injected with PEG (I-K) or RGD C'Dots (L-N) 45 minutes before imaging with endogenous third harmonic generation signal. Analysis of the signal intensity across a linear profile of representative cells (white line) showed that the THG signal, which highlights material interfaces (i.e. matrix/fluid boundary), was external to both PEG (O) and RGD C'Dot signal (P).

cholesterol-depleting MβCD in lowering initial PEG-C'Dot uptake into osteocytes for both sexes (Figure 3). The same images for RGD- and cell penetrating TAT-C'Dots have less obvious trends in initial signal uptake. Quantification of all 10 acute imaging time points for each group allowed for statistical assessment of the impact of endocytic drugs on acute C'Dot uptake and clearance (Figure 4). Overall, there are some clear trends in this acute (behavior in first 30 min) data. First, consistent with findings of our initial report (49), uptake and retention over the first 30 min of C'Dots without any drug administration (i.e., in PBS) is generally higher in female than in male mice. Second, MβCD leads to lowering of C'Dot uptake relative to PBS controls in male and female mice across all C'Dots tested, except for TAT-C'Dots in male mice. Third, the role of Dyngo4a in modulating uptake and retention over the first 30 min is reversed between male and female mice, except for TAT-C'Dots. Linear regressions of the C'Dot clearance profiles spotlight changes in both initial uptake and rate of clearance, quantified as the y-intercept and slope, respectively (Figure 4). Looking at the rate of clearance, male mice incubated with MβCD had more PEG-C'Dot signal over time ($p \leq 0.05$) and male mice incubated with Dyngo4a had more RGD-C'Dot signal over time compared to vehicle control ($p \leq 0.0001$). Interestingly, the male RGD-C'Dot group with Dyngo4a pre-incubation was the only drug group with a positive slope. No female groups had significant changes in clearance rate. Looking at initial C'Dot uptake, MBCD and Dyngo pre-incubation led to different y-intercepts across all C'Dot types and sexes. These results support the finding that endocytosis disrupting drugs impact acute C'Dot uptake into and clearance from osteocytes *in vivo*.

3.3 Extended Osteocyte C'Dot Clearance with Endocytic Inhibitors. Changes of the dynamics of C'Dots in osteocytes by endocytic disrupting drugs were further investigated over an extended period up to 2.5 hours. Again, some clear trends can be identified from these data (Supp. Fig. S3). First, the increased uptake and retention of PEG- and RGD-functionalized C'Dots in females relative to male mice is very clear (49). While C'Dots are completely cleared over the first hour in male mice, their signal declines but remains detectable out to the last data point of 2.5 hours in females.

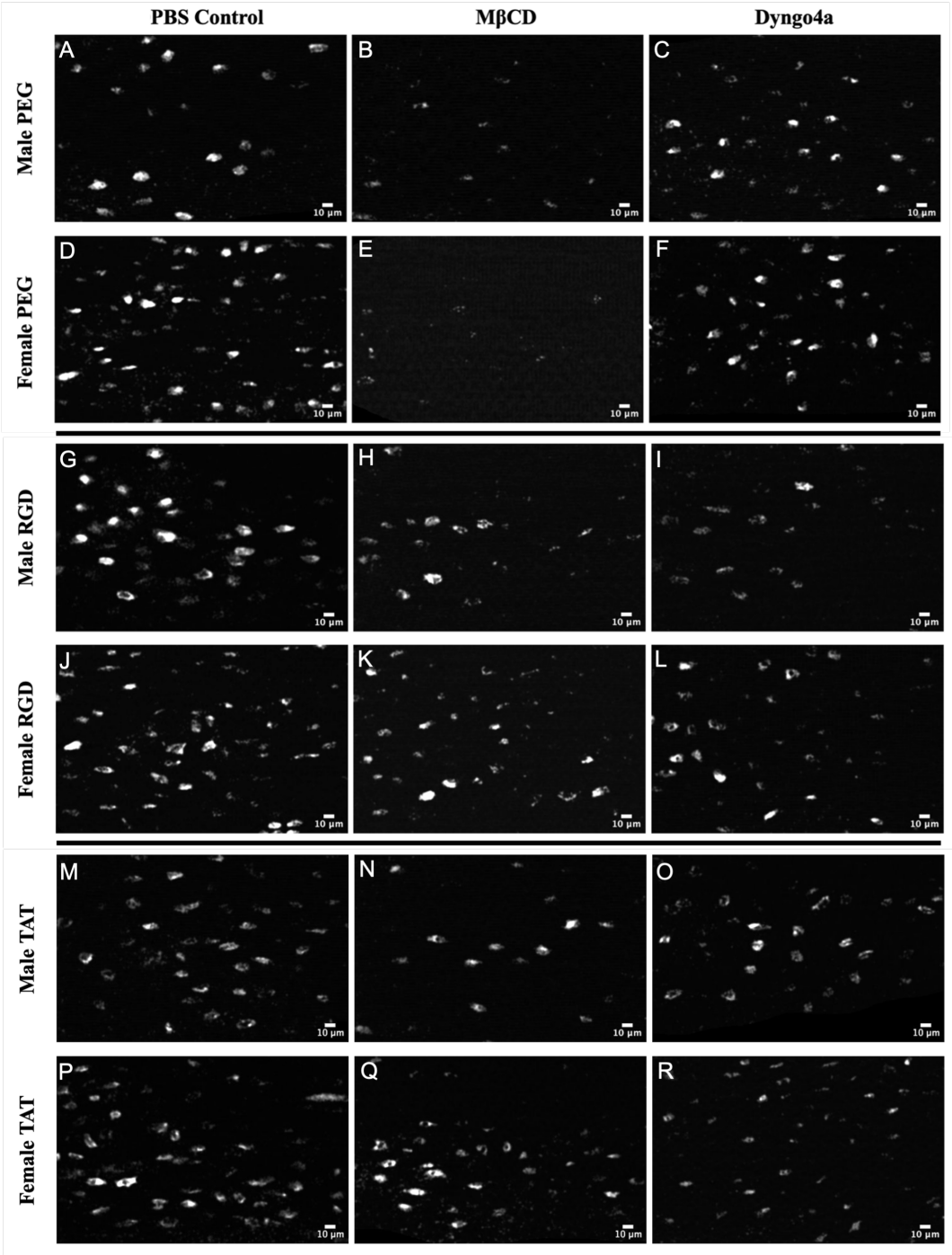

Fig. 3. Representative single-frame images of acute C'Dot uptake into cortical bone osteocytes under different endocytic drug conditions. Images were taken after a 30-minute incubation of drug or PBS control followed by a 5-minute incubation of PEG- (A-F), RGD- (G-L), or TAT- (M-R) C'Dots. Complete z-stacks from each time point were used to quantify the amount of osteocyte nanoparticle uptake over time. Scale bar = 10µm.

Second, uptake and retention are categorically different for TAT-C'Dots in both sexes, exhibiting high and sustained signal for the entire experiment. Third, substantial modulation of uptake and retention is observed as a function of drug treatment. MβCD pre-incubation resulted in an increase in PEG-C'Dot signal in males, and an increase in RGD-C'Dot signal in both males and females (Supp. Fig. S3, 2-Way ANOVA). Interestingly, the opposite effect was seen in the TAT-C'Dot groups, with MβCD resulting in a decrease in signal in both males and females ($p \leq 0.05$). Five out of the six MβCD treated groups had a significantly different clearance profile compared to untreated control. The one outlier (female PEG-C'Dots) had sizeable inter-animal variation, which resulted in low statistical power. In regression analysis, slopes between control and MβCD treated groups were different for all groups except male PEG-C'Dots (Supp. Table 1, Supp. Fig.

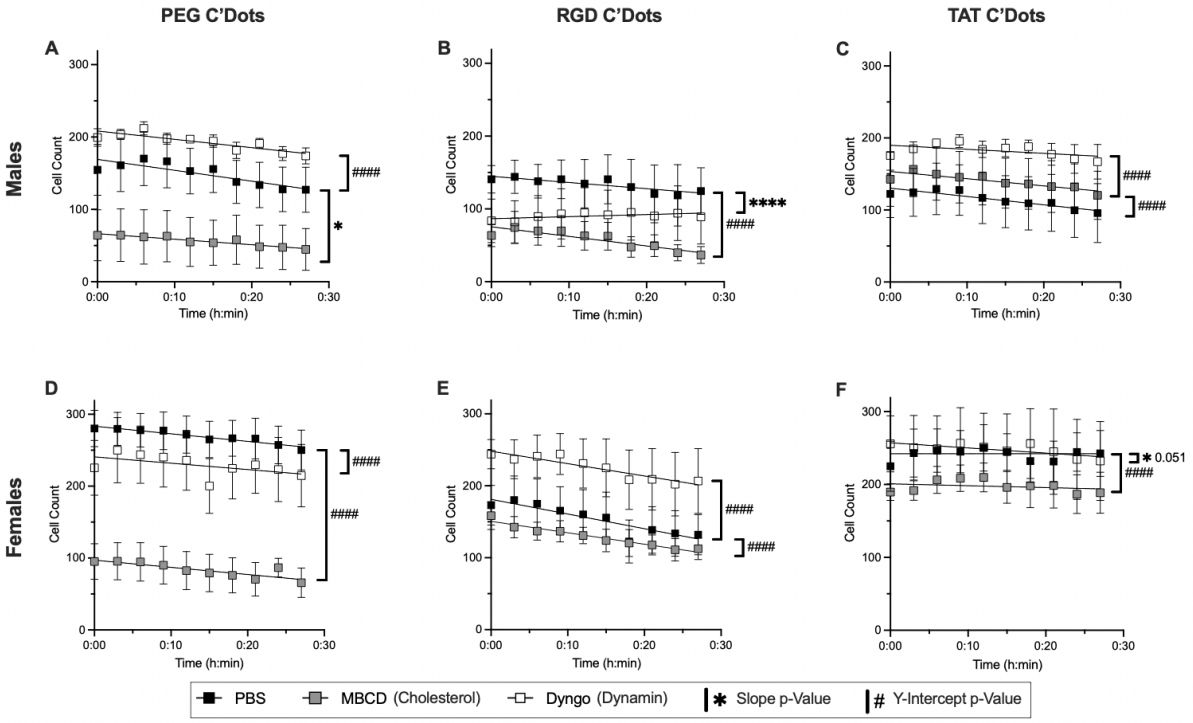

Fig. 4. Quantification of acute C'Dot uptake and retention in cortical bone osteocytes *in vivo*. Grouped by sex and C'Dot type, simple linear regressions measure the impact of endocytic drugs on C'Dot uptake in osteocytes over time. Male groups are graphed on the top row (A-C) and female groups are graphed on the bottom row (D-F). Statistical measurements compare drug groups to PBS control within each panel. A significant difference in slope is shown as *p≤0.05, **p≤0.01, ***p≤0.001, ****p≤0.0001. A significant difference in y-intercept is shown as #p≤0.05, ##p≤0.01, ###p≤0.001, ####p≤0.0001. Error = SEM.

S3). The MβCD treated male PEG-C'Dot group did however have a distinct y-intercept from control ($p<0.0001$). These results support the strong role of cholesterol-mediated uptake and clearance across C'Dot functionalization and sex. Compared to the large impact of MβCD's cholesterol depletion, Dyngo4a's dynamin inhibition only modulated the extended uptake and clearance metabolism of one group compared to untreated control: male RGD-C'Dots (Supp. Fig. S3, $p\leq0.0001$, 2-Way ANOVA). Untreated RGD-C'Dot males lost signal after only an hour of imaging, but Dyngo4a caused the signal to increase dramatically and to be maintained until the end of the imaging experiment. Females treated with Dyngo4a instead experienced a slight decrease in signal, indicating a sexually dimorphic response to the drug. The unique response of RGD-C'Dots in males is confirmed by mixed model analysis (Supp. Fig. S6). However, regression analysis indicated that the slopes between control and Dyngo4a treated groups were different for RGD-C'Dots in both males and females, confirming the role of dynamin in receptor-targeted nanoparticle uptake and clearance (Supp. Table 1). PEG- and TAT-C'Dot groups had no differences in slope but the y-intercepts between Dyngo4a and control groups were distinct (Supp. Table 1). Together these data suggest that the impact of dynamin on nanoparticle uptake and clearance depends on functionalization. While linear regressions provide useful data on slope and y-intercepts, they do not fit all data sets. Due to the relatively low R2 fits, we also ran One-Phase Decay (OPD) regression analysis. The non-linear decay curve created much better fits for a majority of groups (Supp. Table 1). For each C'Dot treatment group, we tested whether a linear or OPD fit was preferred. Untargeted PEG-C'Dots were better represented by OPD for all except the MβCD females (Supp. Table 2). Integrin-targeted RGD-C'Dot groups were more varied, with both Dyngo4a males and MβCD females better represented by a linear fit. Compellingly, the membrane penetrating TAT-C'Dots was best represented by a linear fit across all drug groups. Comparison between linear and OPD fits provides insight into C'Dot clearance kinetics and the impact of drugs on specific C'Dot types. Together, the results from the extended clearance study start to form a coherent picture: Dyngo4a has a major impact on RGD-C'Dots, but only in males while MβCD impacts C'Dot osteocyte metabolism more broadly, across C'Dot types and group sexes.

3.4 Combining Acute and Extended Studies of Osteocyte Nanoparticle Uptake and Clearance. It is further instructive to display the overall kinetics of C'Dot uptake and clearance across both acute and extended time periods in single plots (Figure 5). Starting with the untreated groups, PEG- and RGD-C'Dot clearance follows an expected pattern of continuous decay for both males and females (Figure 5). TAT-C'Dots have a much higher total cellular uptake in the extended study for both males and females, confirming the efficacy of TAT-C'Dot design as membrane-penetrating nanoparticles, evading endocytic recycling and degradation. Pre-incubation with MβCD resulted in an increase in extended signal for nearly all groups compared to

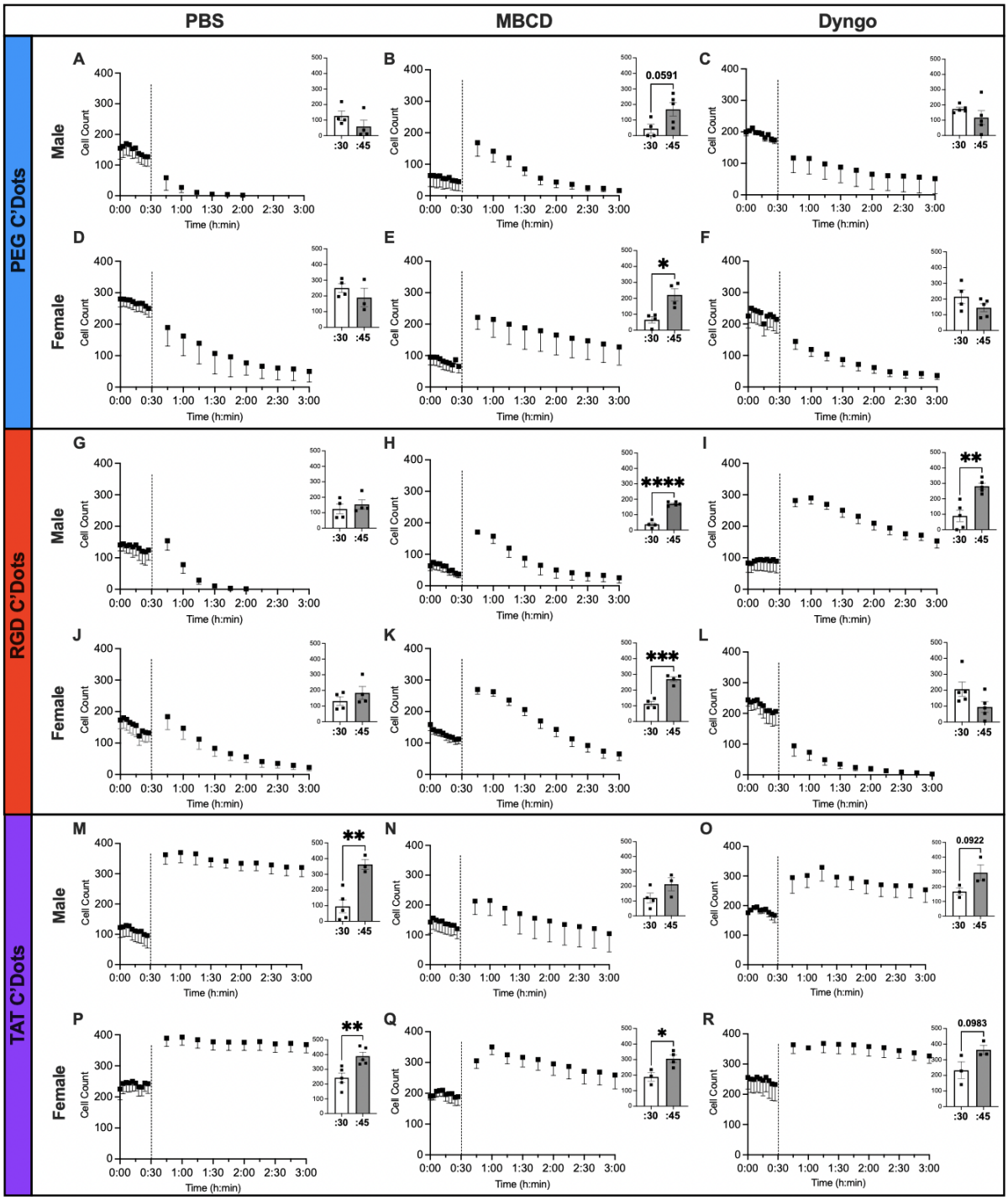

Fig. 5. Acute and extended nanoparticle clearance in cortical bone osteocytes over time. The acute study for each drug and C'Dot group is shown in the first 30 minutes of each graph, to the left of the dotted black line. The extended study is shown following the dotted black line. PEG C'Dot groups are highlighted in blue on the left (A-F), RGD C'Dot groups are highlighted in red (G-L), and TAT C'Dot groups are highlighted in purple (M-R). For each set of studies, a student's T-test was performed between the final acute timepoint and the initial extended timepoint (inset for each graph, *$p \leq 0.05$, **$p \leq 0.01$, ***$p \leq 0.001$, ****$p \leq 0.0001$, Error = SEM, n=3-5/group).

the acute study results (Figure 5, $p \leq 0.05$). MβCD male PEG- and TAT-C'Dots groups did not reach significance although the male PEG-C'Dot group was close (p=0.0591). Pre-incubation with Dyngo4a resulted in an increase in extended signal for only one group, the male RGD-C'Dot group (Figure 4, $p \leq 0.01$). There was no impact of Dyngo4a on either PEG-C'Dot group. Notably, both TAT-C'Dot groups appear similar to their control, confirming the impact of Dyngo4a on receptor-targeted C'Dots alone. Comparing male and female results across the combined clearance studies, there are 3 major takeaways. First, in the untreated groups, male clearance is more rapid than female clearance

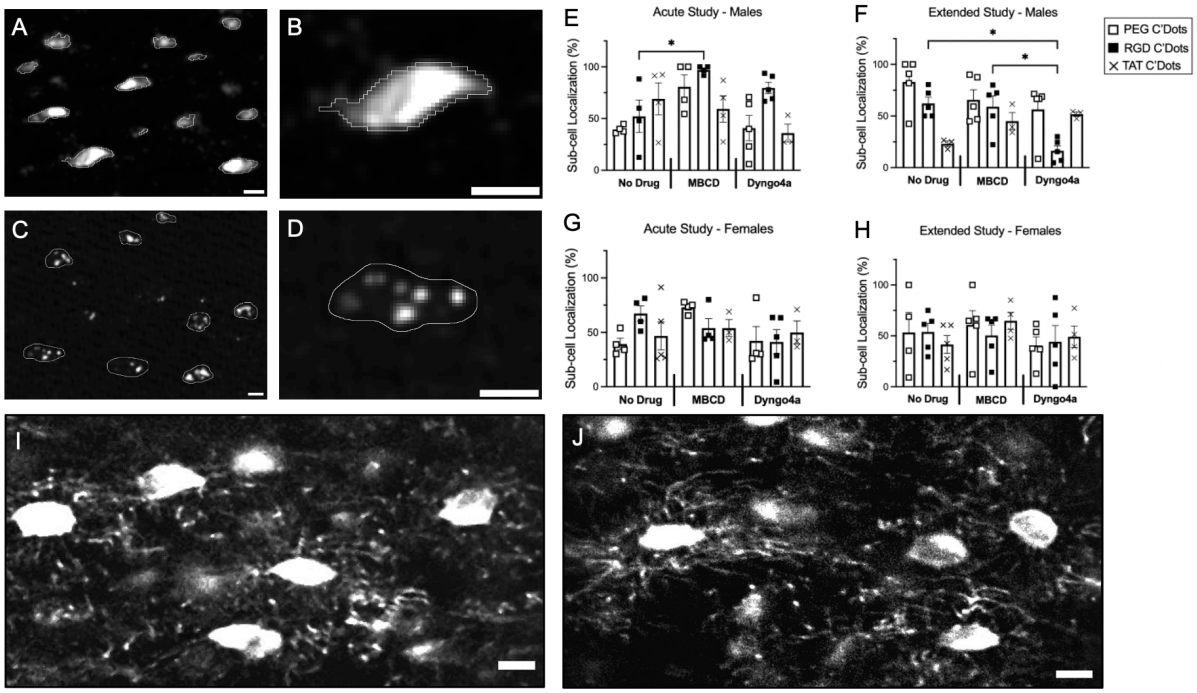

Fig. 6. Subcellular localization of C'Dots within osteocytes *in vivo*. C'Dot signal within osteocytes can be diffuse and saturated (A-B) or discrete and punctate (C-D). Quantification of the percentage of cells with discrete subcellular signal at the first acute and first extended experimental imaging timepoints under different drug conditions is shown in panels E-H. Acute males (E), extended males (F), acute females (G), and extended females (H). Student's T-Tests compare each of the groups within each plot (*$p \leq 0.05$, Error = SEM). Osteocyte dendritic networks can also be observed with C'Dot subcellular signal with a short (5-minute) incubation time of PEG (I) or RGD (J) C'Dots.

with both untargeted and receptor-targeted C'Dots. Second, MβCD application results in a significant increase for both male and female uptake compared to acute data. Third, Dyngo4a application has no impact on females compared to untreated groups while clearance is significantly prolonged in males, specifically for receptor-targeted C'Dots. Sexual dimorphism is confirmed across drug groups in a mixed model analysis (Supp. Fig. S6).

3.5 Subcellular Localization of C'Dots. Apart from the total cell count of osteocytes with C'Dot uptake over time, nanoparticle signal can also be tracked subcellularly. Example images of diffuse and discrete cellular signals are shown in Figure 6. We quantified the percentage of subcellular signal localization at the first imaging time point for both the acute and extended studies. At the acute C'Dot incubation timepoint, discrete subcellular localization of C'Dots was seen in 50% of cells in undrugged groups, with RGD-C'Dots having slightly higher amounts in both males and females (Figure 6). Application of MβCD resulted in an increase in subcellular signal for PEG- and RGD-C'Dot groups in male mice only ($p \leq 0.05$). Dyngo4a application did not result in any difference compared to vehicle control in the acute study. For the extended C'Dot incubation imaging timepoint, discrete subcellular localization of C'Dot signal in undrugged osteocyte cell bodies was again seen in 50% in females but was higher in males, 60-80% (Figure 6). The application of MβCD did not change the percentage of cells with subcellular localization in any group. Pre-incubation with Dyngo4a significantly reduced the number of cells with subcellular localization to 25% in RGD-C'Dot males only (ANOVA, $p \leq 0.05$). No other groups had changes in subcellular localization due to Dyngo4a. Interestingly, female groups with any C'Dot type did not have changes in subcellular localization in response to drug application. Finally, subcellular structures are also visible beyond the osteocyte cell bodies. Using a short C'Dot incubation time, optical zoom, and high frame averaging, the osteocyte dendritic network is visible (Figure 6). The capacity to observe nanoparticles within the dendritic structures in the lacuno-canalicular network in wild-type mice *in vivo* is a novel result that further confirms the ability of C'Dots to act as a powerful tool for optical intravital imaging and analysis.

4. Discussion

The concept of endocytosis has been researched since the late 19th century after phagocytosis was first observed in cells (59, 60). Endocytosis is now considered to be a key regulator of cell sensitivity and responsiveness to its environment as it controls the spatiotemporal composition of the plasma membrane and modulates the localization, number, and availability of transmembrane proteins (61). The sensitivity of neurons depends on precise endocytic control of synaptic receptors (62), and the mechanosensitivity of fibroblasts and neutrophils relies on the internalization and trafficking of integrin proteins (39, 63). Despite the clear physiological importance of endocytosis-mediated cellular sensitivity, details have not been fully established as a physiological paradigm in mechanosensitive cells. We report here new findings that

endocytic pathways can be observed and modulated at the cellular level in real time in living mice *in vivo*. We also report important differences in endocytic dynamics between male and female mice.

Osteocytes, highly mechanosensitive cells that control bone homeostasis while embedded within mineralized bone matrix, have been identified to be mechanosensors in the last 30 years but remain very difficult to study in their natural environment (1, 64–66). Results presented here establish the feasibility of observing uptake and clearance pathways in skeletal tissue *in vivo* using fluorescent nanoparticles and multiphoton microscopy (Supp. Videos 1,2). Ultrasmall fluorescent core-shell silica nanoparticles were successfully utilized as a methodology to assess osteocyte uptake, retention, and clearance activity *in vivo* in the absence and presence of endocytosis disrupting drugs. These data confirm the ability of small molecule endocytosis disruptors to impact osteocyte activity in murine long bone with a local subcutaneous injection at both acute and extended time points.

Endocytosis inhibiting drugs have previously been utilized as drugs in humans (67). The ability to modulate and repair pathological endocytic dysfunction with drugs may be an intriguing option as the medical field shifts towards personalized and targeted cellular medicine. Our results highlight the effect of MβCD across nanoparticle functionalization groups and indicate that cholesterol and lipid raft modulation can impact uptake pathways broadly (Figure 5, Supp. Fig. S3). This aligns with other research on nanoparticle uptake (68) and suggests membrane cholesterol levels are fundamental for a broad range of endocytic pathways (69). In one study, the mechanosensitive response within bone tissue was limited by endocytosis of activated receptors; and when caveolin proteins were disrupted, researchers found increased calcium signaling and mineralization in response to ATP stimulation (70). These findings support the hypothesis that disrupting endocytic pathways involving the internalization of transmembrane proteins may be a novel method for enhancing the mechanosensitive response of bone, a desired outcome in aging and osteoporotic patients. Our findings add to the consensus that membrane cholesterol levels and cholesterol-mediated endocytosis may be a spatiotemporal controller of mechanosensitive proteins and could be an intriguing therapeutic target for modulating bone's response to mechanical stimulation.

Importantly, the dramatic rebound of signal for many of the drug groups between the acute and extended studies implies that the drugs inhibit normal C'Dot uptake initially, which then experiences a rebound as the effects of the drug may be wearing off (Figure 5). *In vitro* literature suggests that MβCD membrane cholesterol depletion is long-lasting with effects maintained for at least 12 hours (71, 72). However, *in vitro* work with Dyngo4a suggests that its effects are much more transient, with all dynamin-mediated endocytosis recovered 30 minutes after drug washout (34). Future work will need to probe the active timeline of these small molecule endocytosis inhibitors *in vivo* and test if they can be used to modulate cellular activity for distinct periods before allowing a return to baseline. It is important to note that during the incubation for the extended clearance study, the mice were allowed normal cage activity compared to the acute incubation where they remained under anesthesia. This ambulation and associated increase in lacuno-canalicular fluid flow may be one cause of changes noted between the acute and extended study. Previous models and *in vivo* experiments have suggested that loading allows for increased oscillatory fluid flow and tracer entry in the lacunar-canalicular system (LCS) (73, 74). Additionally, previous *in vivo* endocytosis experiments have reported an increase in signal intensity over time as trafficking and downstream endocytic vesicle fusion advances (75), which may also explain the increase in signal observed at our extended time points.

C'Dot functionalization provided unique insight into osteocyte endocytic pathways. All three C'Dot types displayed distinct uptake and clearance profiles, especially visible in the extended clearance study. Our positive control of cell penetrating TAT-C'Dots maintained high levels of cell uptake over time, aligning with the hypothesis that these C'Dots evade endocytic trafficking and localize indelibly to the cytoplasm (Figure 5, Supp. Fig. S7). Untargeted PEG-C'Dot uptake was modulated by cholesterol depletion but not by dynamin disruption, which suggests that these nanoparticles are being taken up by non-specific endocytic pathways. Finally, integrin-targeted RGD-C'Dots were highly impacted by Dyngo preincubation, but only in males (Supp. Fig. S5). This indicates that dynamin GTPase activity is critical for rapid clearance and subcellular localization of integrin targeted nanoparticles only in male mice. This information is especially interesting in light of the critical role of integrins in osteocyte mechanosensitivity both *in vitro* and *in vivo* (5, 8, 76–79).

Sex differences were not expected in a cellular level study of endocytosis, but our results depict a paradigm of sex differences in osteocyte C'Dot uptake and clearance. At baseline levels, untargeted and integrin-targeted C'Dot clearance varied between the sexes (Figure 5). Drug treatment also had a sex-specific impact: cholesterol modulated both male and female receptor-mediated endocytosis while dynamin only modulated male dynamics. Given the ubiquity of endocytosis mechanisms generally, it is intriguing that the integrin-targeting RGD-C'Dot clearance dynamics were sexually dimorphic. It suggests that the canonical endocytic pathway of clathrin-mediated endocytosis may not play a large role in female osteocyte nanoparticle metabolism. Subcellular localization of C'Dots was also different between the sexes (Figure 6). While the resolution of our current imaging modality does not allow a claim for visualization of endosomes or lysosomes, the observed punctate signal may represent a more ordered or compact uptake compared to the diffuse cell signal. This suggests that cholesterol and dynamin inhibition may perturb normal vesicular packaging of nanoparticles during uptake at different time points in males. Together, our results imply sexual dimorphism as a paradigm for endocytic mechanisms that has not been previously identified. Future work will need to investigate if there is a differential expression of

endocytic components like dynamin between males and females at the cellular level.

Overall, these results represent the first quantification of a novel platform to interrogate live endocytosis dynamics *in vivo*. Our studies directly motivate future work to assess the impact of endocytic disruption and mechanosensitive protein availability on osteocyte mechanosensitivity. Future studies in our lab will interrogate this question, observing the downstream mechanosensitive response of osteocytes to endocytic disruptors *in vivo*. If localization and availability of mechanosensitive proteins can be controlled, pharmacological disruption of specific pathways may be a new way to modulate cellular reaction to mechanical stimulation *in vivo*. Additionally, the observed sexual dimorphism in endocytic pathway utilization is an intriguing and unexpected result that deserves further consideration within the scientific community.

ACKNOWLEDGEMENTS

Thank you to the Weill Hall CARE staff and Karly Hooper for maintaining the mouse colonies used in these experiments. Thanks to Chris Schaffer and Nozomi Nishimura for access to their 3-Photon microscope and to Samantha Bratcher for assisting with 3-Photon image collection. This work was supported by the Department of Biomedical Engineering at Cornell University.

Bibliography

1. Bonewald, L. F. The amazing osteocyte. *Journal of Bone and Mineral Research* **26**, 229–238 (2011). URL https://onlinelibrary.wiley.com/doi/abs/10.1002/jbmr.320. _eprint: https://onlinelibrary.wiley.com/doi/pdf/10.1002/jbmr.320.
2. Dallas, S. L., Prideaux, M. & Bonewald, L. F. The osteocyte: an endocrine cell ... and more. *Endocrine Reviews* **34**, 658–690 (2013).
3. Schaffler, M. B. & Kennedy, O. D. Osteocyte Signaling in Bone. *Current Osteoporosis Reports* **10**, 118–125 (2012). URL https://www.ncbi.nlm.nih.gov/pmc/articles/PMC3366431/.
4. Klein-Nulend, J., Bakker, A. D., Bacabac, R. G., Vatsa, A. & Weinbaum, S. Mechanosensation and transduction in osteocytes. *Bone* **54**, 182–190 (2013).
5. McNamara, L., Majeska, R., Weinbaum, S., Friedrich, V. & Schaffler, M. Attachment of Osteocyte Cell Processes to the Bone Matrix. *The Anatomical Record* **292**, 355–363 (2009). URL https://onlinelibrary.wiley.com/doi/abs/10.1002/ar.20869. _eprint: https://onlinelibrary.wiley.com/doi/pdf/10.1002/ar.20869.
6. Wang, Y., McNamara, L. M., Schaffler, M. B. & Weinbaum, S. A model for the role of integrins in flow induced mechanotransduction in osteocytes. *Proceedings of the National Academy of Sciences* **104**, 15941–15946 (2007). URL https://www.pnas.org/doi/abs/10.1073/pnas.0707246104. Publisher: Proceedings of the National Academy of Sciences.
7. Cabahug-Zuckerman, P. *et al.* Potential role for a specialized β3 integrin-based structure on osteocyte processes in bone mechanosensation. *Journal of Orthopaedic Research* **36**, 642–652 (2018). URL https://onlinelibrary.wiley.com/doi/abs/10.1002/jor.23792. _eprint: https://onlinelibrary.wiley.com/doi/pdf/10.1002/jor.23792.
8. Haugh, M. G., Vaughan, T. J. & McNamara, L. M. The role of integrin αVβ3 in osteocyte mechanotransduction. *Journal of the Mechanical Behavior of Biomedical Materials* **42**, 67–75 (2015). URL https://www.sciencedirect.com/science/article/pii/S1751616114003403.
9. Miyauchi, A. *et al.* AlphaVbeta3 integrin ligands enhance volume-sensitive calcium influx in mechanically stretched osteocytes. *Journal of Bone and Mineral Metabolism* **24**, 498–504 (2006).
10. Xu, H. *et al.* Oscillatory fluid flow elicits changes in morphology, cytoskeleton and integrin-associated molecules in MLO-Y4 cells, but not in MC3T3-E1 cells. *Biological Research* **45**, 163–169 (2012). URL http://www.scielo.cl/scielo.php?script=sci_abstract&pid=S0716-97602012000200008&lng=es&nrm=iso&tlng=en. Publisher: Sociedad de Biología de Chile.
11. Cluzel, C. *et al.* The mechanisms and dynamics of αvβ3 integrin clustering in living cells. *Journal of Cell Biology* **171**, 383–392 (2005). URL https://doi.org/10.1083/jcb.200503017.
12. Moreno-Layseca, P., Icha, J., Hamidi, H. & Ivaska, J. Integrin trafficking in cells and tissues. *Nature Cell Biology* **21**, 122–132 (2019). URL https://www.nature.com/articles/s41556-018-0223-z. Number: 2 Publisher: Nature Publishing Group.
13. Paul, N. R., Jacquemet, G. & Caswell, P. T. Endocytic Trafficking of Integrins in Cell Migration. *Current Biology* **25**, R1092–R1105 (2015). URL https://www.sciencedirect.com/science/article/pii/S0960982215011604.
14. Cullen, P. J. & Steinberg, F. To degrade or not to degrade: mechanisms and significance of endocytic recycling. *Nature Reviews Molecular Cell Biology* **19**, 679–696 (2018). URL https://www.nature.com/articles/s41580-018-0053-7. Publisher: Nature Publishing Group.
15. Mani, I. & Singh, V. An overview of receptor endocytosis and signaling. *Progress in Molecular Biology and Translational Science* **194**, 1–18 (2023).
16. Michl, J. Receptor mediated endocytosis. *The American Journal of Clinical Nutrition* **33**, 2462–2471 (1980).
17. Kotowski, S. J., Hopf, F. W., Seif, T., Bonci, A. & von Zastrow, M. Endocytosis promotes rapid dopaminergic signaling. *Neuron* **71**, 278–290 (2011).
18. Nguyen, T. H., Qiu, X., Sun, J. & Meunier, F. A. Bulk endocytosis at neuronal synapses. *Science China Life Sciences* **57**, 378–383 (2014). URL https://doi.org/10.1007/s11427-014-4636-z.
19. Zimmermann, H. *et al.* The synaptic vesicle membrane: Origin, axonal distribution, protein components, exocytosis and recycling. *Cell Biology International Reports* **13**, 993–1006 (1989). URL https://www.sciencedirect.com/science/article/pii/0309165189900155.
20. Mousavi, S. A., Malerød, L., Berg, T. & Kjeken, R. Clathrin-dependent endocytosis. *The Biochemical Journal* **377**, 1–16 (2004).
21. Lee, Y. D. *et al.* Caveolin-1 regulates osteoclastogenesis and bone metabolism in a sex-dependent manner. *The Journal of Biological Chemistry* **290**, 6522–6530 (2015).
22. Rubin, J. *et al.* Caveolin-1 Knockout Mice Have Increased Bone Size and Stiffness. *Journal of Bone and Mineral Research* **22**, 1408–1418 (2007). URL https://onlinelibrary.wiley.com/doi/abs/10.1359/jbmr.070601. _eprint: https://onlinelibrary.wiley.com/doi/pdf/10.1359/jbmr.070601.
23. Qiu, T. *et al.* TGF-β type II receptor phosphorylates PTH receptor to integrate bone remodelling signalling. *Nature Cell Biology* **12**, 224–234 (2010). URL https://www.nature.com/articles/ncb2022. Number: 3 Publisher: Nature Publishing Group.
24. Zhao, H. Membrane Trafficking in Osteoblasts and Osteoclasts: New Avenues for Understanding and Treating Skeletal Diseases. *Traffic* **13**, 1307–1314 (2012). URL https://onlinelibrary.wiley.com/doi/abs/10.1111/j.1600-0854.2012.01395.x. _eprint: https://onlinelibrary.wiley.com/doi/pdf/10.1111/j.1600-0854.2012.01395.x.
25. Gagliardi, M., Piddini, E. & Vincent, J.-P. Endocytosis: A Positive or a Negative Influence on Wnt Signalling? *Traffic* **9**, 1–9 (2008). URL https://onlinelibrary.wiley.com/doi/abs/10.1111/j.1600-0854.2007.00662.x. _eprint: https://onlinelibrary.wiley.com/doi/pdf/10.1111/j.1600-0854.2007.00662.x.
26. Vaccari, T., Lu, H., Kanwar, R., Fortini, M. E. & Bilder, D. Endosomal entry regulates Notch receptor activation in Drosophila melanogaster. *Journal of Cell Biology* **180**, 755–762 (2008). URL https://doi.org/10.1083/jcb.200708127.
27. Lemmon, S. K. & Jones, E. W. Clathrin requirement for normal growth of yeast. *Science (New York, N.Y.)* **238**, 504–509 (1987).
28. Myers, M. D. & Payne, G. S. Clathrin, adaptors and disease: insights from the yeast Saccharomyces cerevisiae. *Frontiers in Bioscience (Landmark Edition)* **18**, 862–891 (2013).
29. Burgess, J. *et al.* AP-1 and clathrin are essential for secretory granule biogenesis in Drosophila. *Molecular Biology of the Cell* **22**, 2094–2105 (2011). URL https://www.molbiolcell.org/doi/full/10.1091/mbc.e11-01-0054. Publisher: American Society for Cell Biology (mboc).
30. Ganapathy, A. S. *et al.* AP2M1 mediates autophagy-induced CLDN2 (claudin 2) degradation through endocytosis and interaction with LC3 and reduces intestinal epithelial tight junction permeability. *Autophagy* **18**, 2086–2103 (2022).
31. Heilker, R., Manning-Krieg, U., Zuber, J. F. & Spiess, M. In vitro binding of clathrin adaptors to sorting signals correlates with endocytosis and basolateral sorting. *The EMBO Journal* **15**, 2893–2899 (1996). URL https://www.ncbi.nlm.nih.gov/pmc/articles/PMC450227/.
32. Mettlen, M., Pucadyil, T., Ramachandran, R. & Schmid, S. Dissecting dynamin's role in clathrin-mediated endocytosis. *Biochemical Society Transactions* **37**, 1022–1026 (2009). URL https://doi.org/10.1042/BST0371022.
33. Redlingshöfer, L. *et al.* Clathrin light chain diversity regulates membrane deformation in vitro and synaptic vesicle formation in vivo. *Proceedings of the National Academy of Sciences of the United States of America* **117**, 23527–23538 (2020).
34. McCluskey, A. *et al.* Building a Better Dynasore: The Dyngo Compounds Potently Inhibit Dynamin and Endocytosis. *Traffic* **14**, 1272–1289 (2013). URL https://onlinelibrary.wiley.com/doi/abs/10.1111/tra.12119. _eprint: https://onlinelibrary.wiley.com/doi/pdf/10.1111/tra.12119.
35. Alanko, J. *et al.* Integrin endosomal signalling suppresses anoikis. *Nature Cell Biology* **17**, 1412–1421 (2015). URL https://www.nature.com/articles/ncb3250. Number: 11 Publisher: Nature Publishing Group.
36. Bass, M. D. *et al.* A syndecan-4 hair trigger initiates wound healing through caveolin- and RhoG-regulated integrin endocytosis. *Developmental Cell* **21**, 681–693 (2011).
37. del Pozo, M. A. *et al.* Phospho-caveolin-1 mediates integrin-regulated membrane domain internalization. *Nature Cell Biology* **7**, 901–908 (2005). URL https://www.nature.com/articles/ncb1293. Number: 9 Publisher: Nature Publishing Group.
38. Shi, F. & Sottile, J. Caveolin-1-dependent β1 integrin endocytosis is a critical regulator of fibronectin turnover. *Journal of Cell Science* **121**, 2360–2371 (2008). URL https://doi.org/10.1242/jcs.014977.
39. Gu, Z., Noss, E. H., Hsu, V. W. & Brenner, M. B. Integrins traffic rapidly via circular dorsal ruffles and macropinocytosis during stimulated cell migration. *The Journal of Cell Biology* **193**, 61–70 (2011).
40. Rahn, E., Petermann, P., Hsu, M.-J., Rixon, F. J. & Knebel-Mörsdorf, D. Entry pathways of herpes simplex virus type 1 into human keratinocytes are dynamin- and cholesterol-dependent. *PloS One* **6**, e25464 (2011).
41. Savio, L. E. B. *et al.* P2X7 receptor activation increases expression of caveolin-1 and formation of macrophage lipid rafts, thereby boosting CD39 activity. *Journal of Cell Science* **133**, jcs237560 (2020). URL https://www.ncbi.nlm.nih.gov/pmc/articles/PMC7063835/.
42. Mahammad, S. & Parmryd, I. Cholesterol Depletion Using Methyl-β-cyclodextrin. In Owen, D. M. (ed.) *Methods in Membrane Lipids*, Methods in Molecular Biology, 91–102 (Springer, New York, NY, 2015). URL https://doi.org/10.1007/978-1-4939-1752-5_8.
43. Maza, P. K. & Suzuki, E. Histoplasma capsulatum-Induced Cytokine Secretion in Lung Ep-

ithelial Cells Is Dependent on Host Integrins, Src-Family Kinase Activation, and Membrane Raft Recruitment. *Frontiers in Microbiology* **7**, 580 (2016).
44. Weigert, R. Imaging the Dynamics of Endocytosis in Live Mammalian Tissues. *Cold Spring Harbor Perspectives in Biology* **6**, a017012 (2014). URL https://www.ncbi.nlm.nih.gov/pmc/articles/PMC3970414/.
45. Dunn, K. W. *et al.* Functional studies of the kidney of living animals using multicolor two-photon microscopy. *American Journal of Physiology-Cell Physiology* **283**, C905–C916 (2002). URL https://journals.physiology.org/doi/full/10.1152/ajpcell.00159.2002. Publisher: American Physiological Society.
46. Martins, J. R. *et al.* Intravital kidney microscopy: entering a new era. *Kidney International* **100**, 527–535 (2021).
47. Masedunskas, A. & Weigert, R. Intravital two-photon microscopy for studying the uptake and trafficking of fluorescently conjugated molecules in live rodents. *Traffic (Copenhagen, Denmark)* **9**, 1801–1810 (2008).
48. Lewis, K. J. *et al.* Osteocyte calcium signals encode strain magnitude and loading frequency in vivo. *Proceedings of the National Academy of Sciences* **114**, 11775–11780 (2017). URL https://www.pnas.org/doi/abs/10.1073/pnas.1707863114. Publisher: Proceedings of the National Academy of Sciences.
49. Matthews, M. D., Cook, E., Naguib, N., Wiesner, U. B. & Lewis, K. J. Intravital imaging of osteocyte integrin dynamics with locally injectable fluorescent nanoparticles. *Bone* **174**, 116830 (2023). URL https://www.sciencedirect.com/science/article/pii/S8756328223001631.
50. Chen, T.-W. *et al.* Ultra-sensitive fluorescent proteins for imaging neuronal activity. *Nature* **499**, 295–300 (2013). URL https://www.ncbi.nlm.nih.gov/pmc/articles/PMC3777791/.
51. Lu, Y. *et al.* DMP1-targeted Cre expression in odontoblasts and osteocytes. *Journal of Dental Research* **86**, 320–325 (2007).
52. Ma, K. *et al.* Control of Ultrasmall Sub-10 nm Ligand-Functionalized Fluorescent Core–Shell Silica Nanoparticle Growth in Water. *Chemistry of Materials* **27**, 4119–4133 (2015). URL https://doi.org/10.1021/acs.chemmater.5b01222. Publisher: American Chemical Society.
53. Ma, K., Zhang, D., Cong, Y. & Wiesner, U. Elucidating the Mechanism of Silica Nanoparticle PEGylation Processes Using Fluorescence Correlation Spectroscopies. *Chemistry of Materials* **28**, 1537–1545 (2016). URL https://doi.org/10.1021/acs.chemmater.6b00030. Publisher: American Chemical Society.
54. Chen, F. *et al.* Cancer-Targeting Ultrasmall Silica Nanoparticles for Clinical Translation: Physicochemical Structure and Biological Property Correlations. *Chemistry of materials : a publication of the American Chemical Society* **29**, 8766–8779 (2017). URL https://www.ncbi.nlm.nih.gov/pmc/articles/PMC5679295/.
55. Choi, J. *et al.* Core-shell silica nanoparticles as fluorescent labels for nanomedicine. *Journal of Biomedical Optics* **12**, 064007 (2007).
56. Ma, K. & Wiesner, U. Modular and Orthogonal Post-PEGylation Surface Modifications by Insertion Enabling Penta-Functional Ultrasmall Organic-Silica Hybrid Nanoparticles. *Chemistry of Materials* **29**, 6840–6855 (2017). URL https://doi.org/10.1021/acs.chemmater.7b02009. Publisher: American Chemical Society.
57. Horton, N. G. *et al.* In vivo three-photon microscopy of subcortical structures within an intact mouse brain. *Nature Photonics* **7**, 205–209 (2013). URL https://www.nature.com/articles/nphoton.2012.336. Publisher: Nature Publishing Group.
58. Pologruto, T. A., Sabatini, B. L. & Svoboda, K. ScanImage: Flexible software for operating laser scanning microscopes. *BioMedical Engineering OnLine* **2**, 13 (2003). URL https://doi.org/10.1186/1475-925X-2-13.
59. Schmid, S. L., Sorkin, A. & Zerial, M. Endocytosis: Past, Present, and Future. *Cold Spring Harbor Perspectives in Biology* **6**, a022509 (2014). URL https://www.ncbi.nlm.nih.gov/pmc/articles/PMC4292149/.
60. Doherty, G. J. & McMahon, H. T. Mechanisms of endocytosis. *Annual Review of Biochemistry* **78**, 857–902 (2009).
61. Gardinier, J. D. The Diminishing Returns of Mechanical Loading and Potential Mechanisms that Desensitize Osteocytes. *Current Osteoporosis Reports* **19**, 436–443 (2021).
62. Rosendale, M., Jullié, D., Choquet, D. & Perrais, D. Spatial and Temporal Regulation of Receptor Endocytosis in Neuronal Dendrites Revealed by Imaging of Single Vesicle Formation. *Cell Reports* **18**, 1840–1847 (2017). URL https://www.sciencedirect.com/science/article/pii/S2211124717301663.
63. Lawson, M. A. & Maxfield, F. R. Ca2+- and calcineurin-dependent recycling of an integrin to the front of migrating neutrophils. *Nature* **377**, 75–79 (1995). URL https://www.nature.com/articles/377075a0. Number: 6544 Publisher: Nature Publishing Group.
64. Choi, J. U. A., Kijas, A. W., Lauko, J. & Rowan, A. E. The Mechanosensory Role of Osteocytes and Implications for Bone Health and Disease States. *Frontiers in Cell and Developmental Biology* **9** (2022). URL https://www.frontiersin.org/articles/10.3389/fcell.2021.770143.
65. Weinbaum, S., Cowin, S. C. & Zeng, Y. A model for the excitation of osteocytes by mechanical loading-induced bone fluid shear stresses. *Journal of Biomechanics* **27**, 339–360 (1994).
66. Han, Y., Cowin, S. C., Schaffler, M. B. & Weinbaum, S. Mechanotransduction and strain amplification in osteocyte cell processes. *Proceedings of the National Academy of Sciences* **101**, 16689–16694 (2004). URL https://www.pnas.org/doi/abs/10.1073/pnas.0407429101. Publisher: Proceedings of the National Academy of Sciences.
67. Chew, H. Y. *et al.* Endocytosis Inhibition in Humans to Improve Responses to ADCC-Mediating Antibodies. *Cell* **180**, 895–914.e27 (2020).
68. Rothen-Rutishauser, B. *et al.* Quantification of gold nanoparticle cell uptake under controlled biological conditions and adequate resolution. *Nanomedicine* **9**, 607–621 (2014). URL https://www.futuremedicine.com/doi/full/10.2217/nnm.13.24. Publisher: Future Medicine.
69. Rennick, J. J., Johnston, A. P. R. & Parton, R. G. Key principles and methods for studying the endocytosis of biological and nanoparticle therapeutics. *Nature Nanotechnology* **16**, 266–276 (2021). URL https://www.nature.com/articles/s41565-021-00858-8. Publisher: Nature Publishing Group.
70. Gangadharan, V., Nohe, A., Caplan, J., Czymmek, K. & Duncan, R. L. Caveolin-1 regulates P2X7 receptor signaling in osteoblasts. *American Journal of Physiology-Cell Physiology* **308**, C41–C50 (2015). URL https://journals.physiology.org/doi/full/10.1152/ajpcell.00037.2014. Publisher: American Physiological Society.
71. Francis, S. A. *et al.* Rapid reduction of MDCK cell cholesterol by methyl-β-cyclodextrin alters steady state transepithelial electrical resistance. *European Journal of Cell Biology* **78**, 473–484 (1999). URL https://www.sciencedirect.com/science/article/pii/S0171933599800740.
72. Danthi, P. & Chow, M. Cholesterol Removal by Methyl-β-Cyclodextrin Inhibits Poliovirus Entry. *Journal of Virology* **78**, 33–41 (2004). URL https://www.ncbi.nlm.nih.gov/pmc/articles/PMC303393/.
73. Wang, L., Cowin, S. C., Weinbaum, S. & Fritton, S. P. Modeling Tracer Transport in an Osteon under Cyclic Loading. *Annals of Biomedical Engineering* **28**, 1200–1209 (2000). URL https://doi.org/10.1114/1.1317531.
74. Wang, L., Ciani, C., Doty, S. B. & Fritton, S. P. Delineating bone's interstitial fluid pathway in vivo. *Bone* **34**, 499–509 (2004). URL https://www.sciencedirect.com/science/article/pii/S8756328203004216.
75. Sandoval, R. M. & Molitoris, B. A. Quantifying endocytosis in vivo using intravital two-photon microscopy. *Methods in Molecular Biology (Clifton, N.J.)* **440**, 389–402 (2008).
76. Thi, M. M., Suadicani, S. O., Schaffler, M. B., Weinbaum, S. & Spray, D. C. Mechanosensory responses of osteocytes to physiological forces occur along processes and not cell body and require αVβ3 integrin. *Proceedings of the National Academy of Sciences* **110**, 21012–21017 (2013). URL https://www.pnas.org/doi/abs/10.1073/pnas.1321210110. Publisher: Proceedings of the National Academy of Sciences.
77. Qin, L. *et al.* Osteocyte β3 integrin promotes bone mass accrual and force-induced bone formation in mice. *Journal of Orthopaedic Translation* **40**, 58–71 (2023). URL https://www.sciencedirect.com/science/article/pii/S2214031X23000281.
78. Qin, L. *et al.* Osteocyte β1 integrin loss causes low bone mass and impairs bone mechanotransduction in mice. *Journal of Orthopaedic Translation* **34**, 60–72 (2022). URL https://www.ncbi.nlm.nih.gov/pmc/articles/PMC9119859/.
79. Litzenberger, J. B., Tang, W. J., Castillo, A. B. & Jacobs, C. R. Deletion of β1 Integrins from Cortical Osteocytes Reduces Load-Induced Bone Formation. *Cellular and Molecular Bioengineering* **2**, 416–424 (2009). URL https://doi.org/10.1007/s12195-009-0068-4.

Supplementary Information

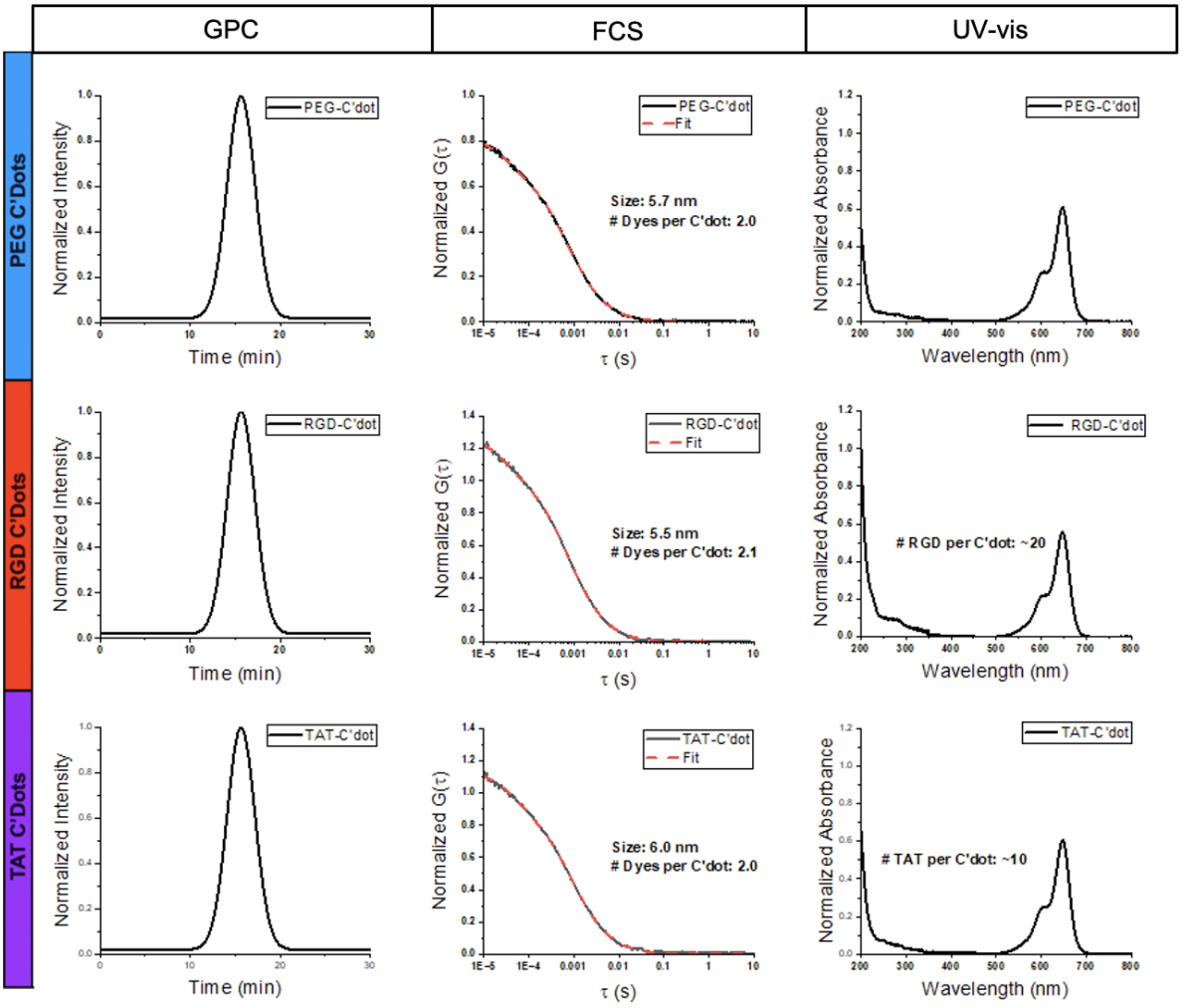

Fig. 7. Figure S1: Characterization of C'Dots using Gel Permeation Chromatography (GPC), Fluorescence Correlation Spectroscopy (FCS) and UV-vis absorbance. The TAT peptide sequence used was: 5-azido-pentanoyl – RKKRRQRRR-NH2. All batches of PEG-C'Dots, RGD-C'Dots and TAT-C'Dots were thoroughly characterized to calculate the number of moieties per particle.

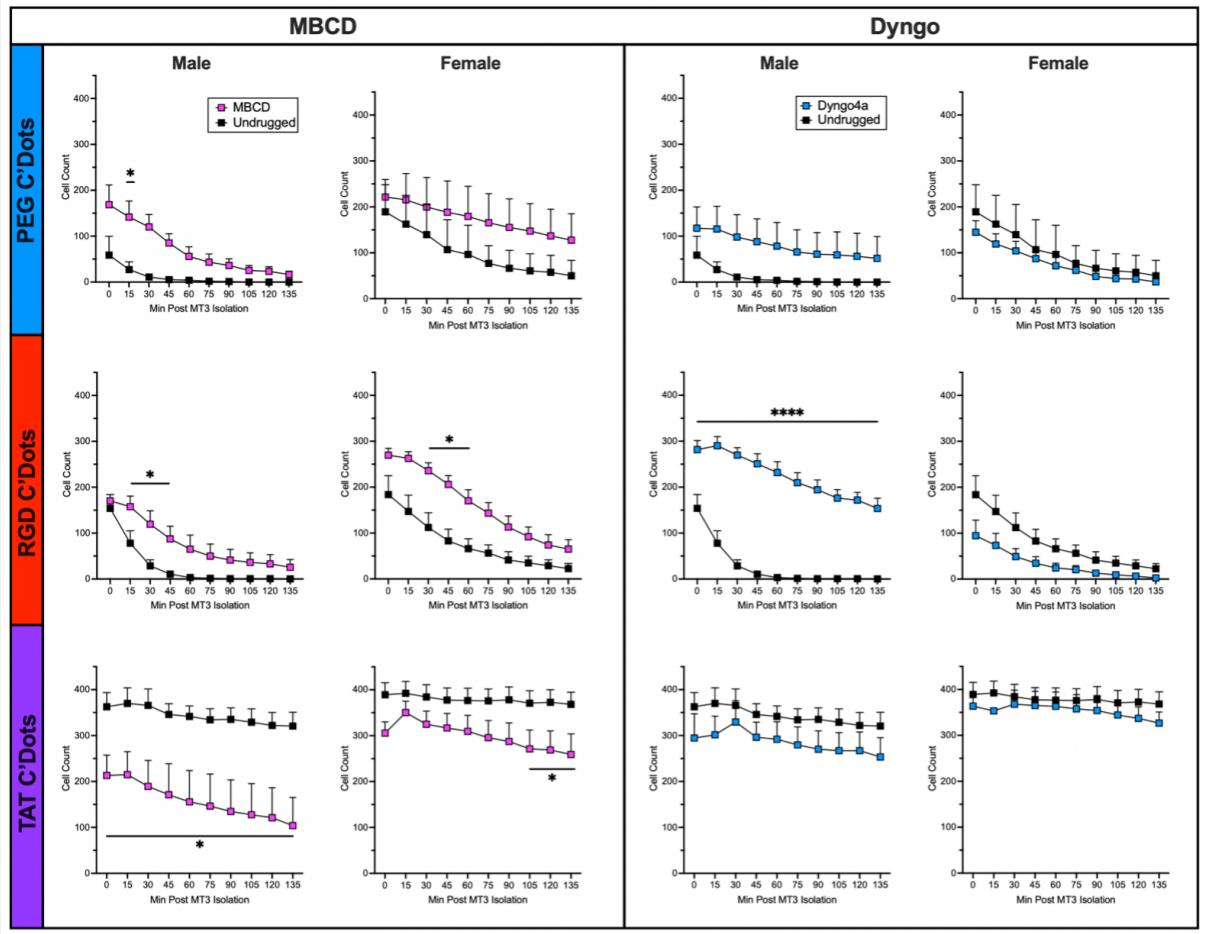

Fig. 8. Figure S2: Kinetics of extended C'Dot clearance in osteocytes under cholesterol disruption and dynamin inhibition. After a 45-minute extended C'Dot incubation, osteocyte uptake of C'Dots under different drug conditions was quantified over time (n=3-5/group). The impact of cholesterol inhibitor (pink) and dynamin inhibitor (blue) compared to untreated control (black) was assessed via 2-way ANOVA. Male data was transformed (Y=log(Y+1)) due to near-zero data points before ANOVA analysis, untransformed data is shown in the graph. Stats compare the drug group to untreated control at each timepoint (*$p \leq 0.05$, **$p \leq 0.01$, ***$p \leq 0.001$, ****$p \leq 0.0001$, Error = SEM).

Fig. 9. Supplmentary Table 1: Linear and One Phase Decay Regression Analysis of Extended C'Dot Clearance. For each C'Dot group, linear regressions (red) and One one-phase decay regressions (blue) are fitted to the data. The impact of dynamin inhibition (Dyngo) and cholesterol depletion (MBCD) on C'Dot uptake and clearance is quantified as changes in linear slope and y-intercept. Bolded sections show significant differences ($p \leq 0.05$). Graphs depicting the regression lines are shown in further supplemental data (Supplemental Figures 2, 3).

C'Dot Treatment Group	Linear Regression (Fit – R^2)	One Phase Decay (Fit – R^2)	Linear Slope vs Dyngo4a	Linear Y-Intercepts vs Dyngo4a	Linear Slope vs MBCD	Linear Y-Intercepts vs MBCD
Male PEG	0.7679	0.9987	p=0.3022	**p<0.0001**	p=0.1226	**p<0.0001**
Male RGD	0.8685	0.9975	**p=0.0018**	-	**p=0.0139**	-
Male TAT	0.9138	0.9176	p=0.7523	**p<0.0001**	**p<0.0001**	-
Female PEG	0.9187	0.9937	p=0.0878	**p=0.0007**	**p=0.0127**	-
Female RGD	0.8976	0.9983	**p=0.0067**	-	**p=0.0022**	-
Female TAT	0.8511	0.8794	p=0.2006	**p<0.0001**	**p=0.0021**	-

Fig. 10. Supplementary Table 2: Comparing Linear and One Phase Decay Regression Analysis for Extended C'Dot Clearance. A comparison test between the two regression curves defines the preferred mode of regression for each C'Dot group. The second column shows the preferred regression without any drug. The third and fourth columns highlight the impact of dynamin inhibition or cholesterol depletion on the preferred regression.

C'Dot Treatment Group	Linear or OPD Preferred?	Linear or OPD Preferred w/Dyngo4a?	Linear or OPD Preferred w/MBCD?
Male PEG	OPD	OPD	OPD
Male RGD	OPD	Linear	OPD
Male TAT	Linear	Linear	Linear
Female PEG	OPD	OPD	Linear
Female RGD	OPD	OPD	Linear
Female TAT	Linear	Linear	Linear

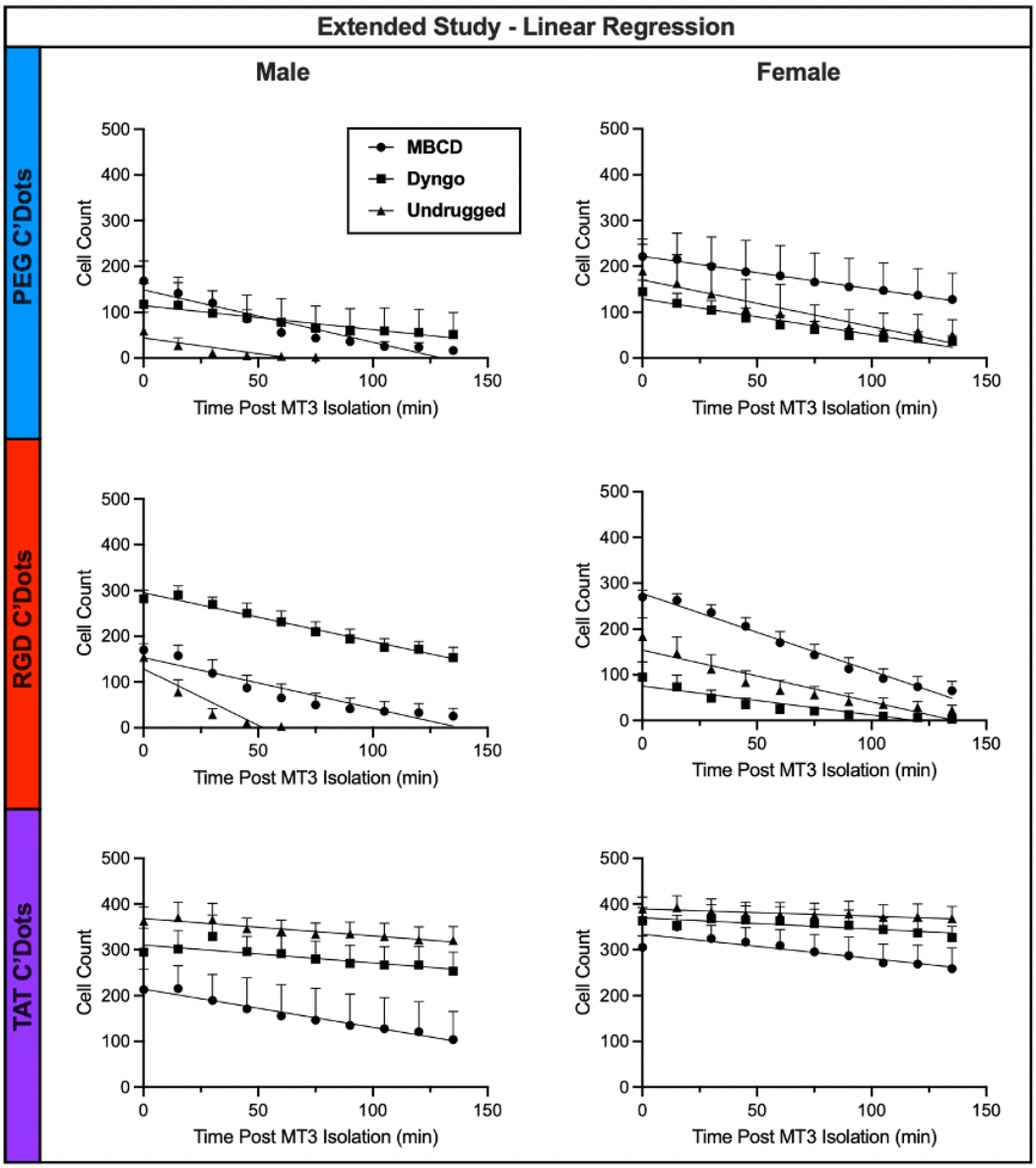

Fig. 11. Figure S3: Simple linear regression lines on extended C'Dot clearance experiment groups. Data points reaching 0 (in Male PEG and RGD groups) were removed before regression analysis. N=3-5/group, Error = SEM.

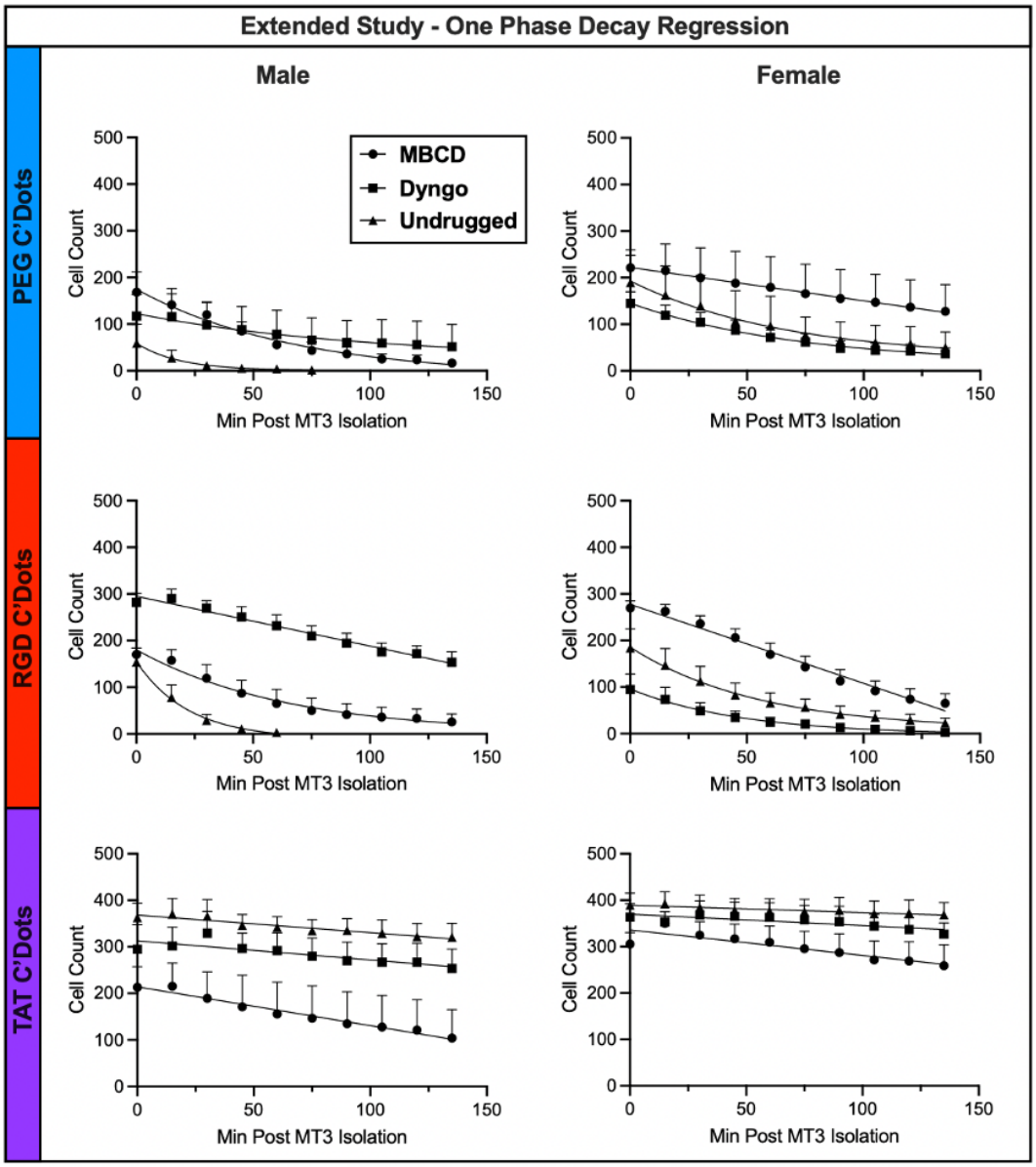

Fig. 12. Figure S4: One phase decay lines on extended C'Dot clearance experiment groups. Data points reaching 0 (in Male PEG and RGD groups) were removed before regression analysis. N=3-5/group, Error = SEM.

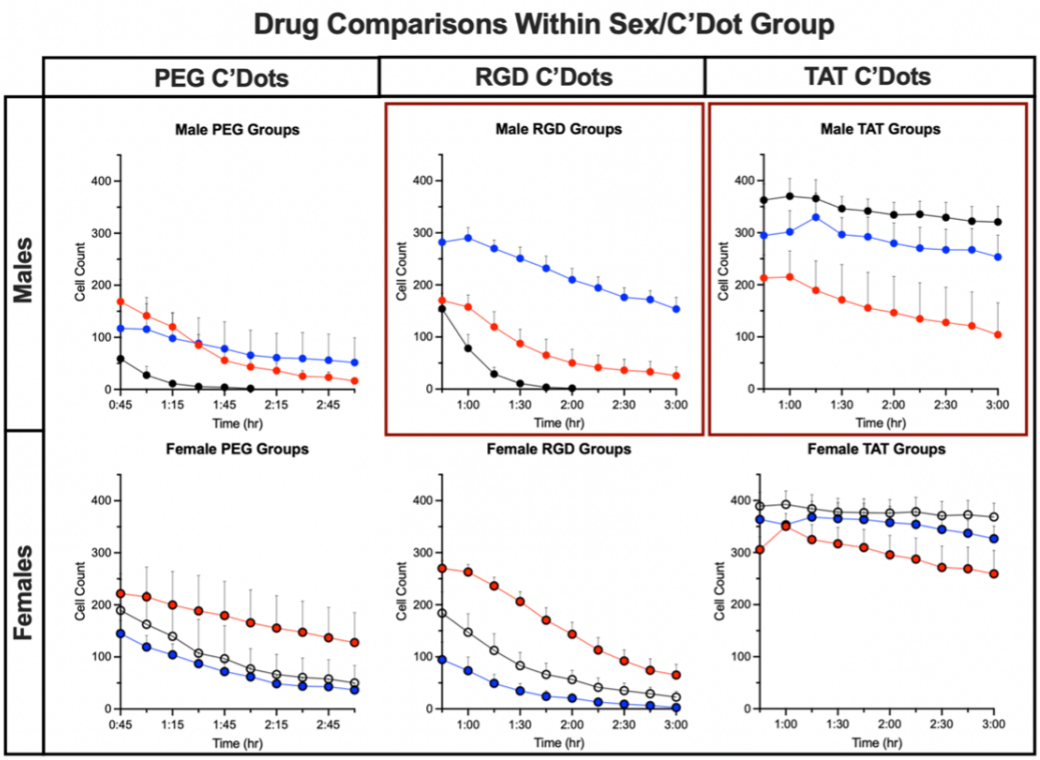

Drug Comparisons	PEG C'Dots	RGD C'Dots	TAT C'Dots
Male	No Drug Differences	Dyngo – MBCD 0.001 Dyngo – PBS 0.0001	MBCD – PBS 0.01
Female	No Drug Differences	No Drug Differences	No Drug Differences

● PBS
● MBCD
● Dyngo

Fig. 13. Figure S5: Plots of mixed model comparisons of drugs within C'Dot and sex groups for the extended clearance data. Comparisons with significant differences are boxed in red. $P \leq 0.05$, Error = ±SEM.

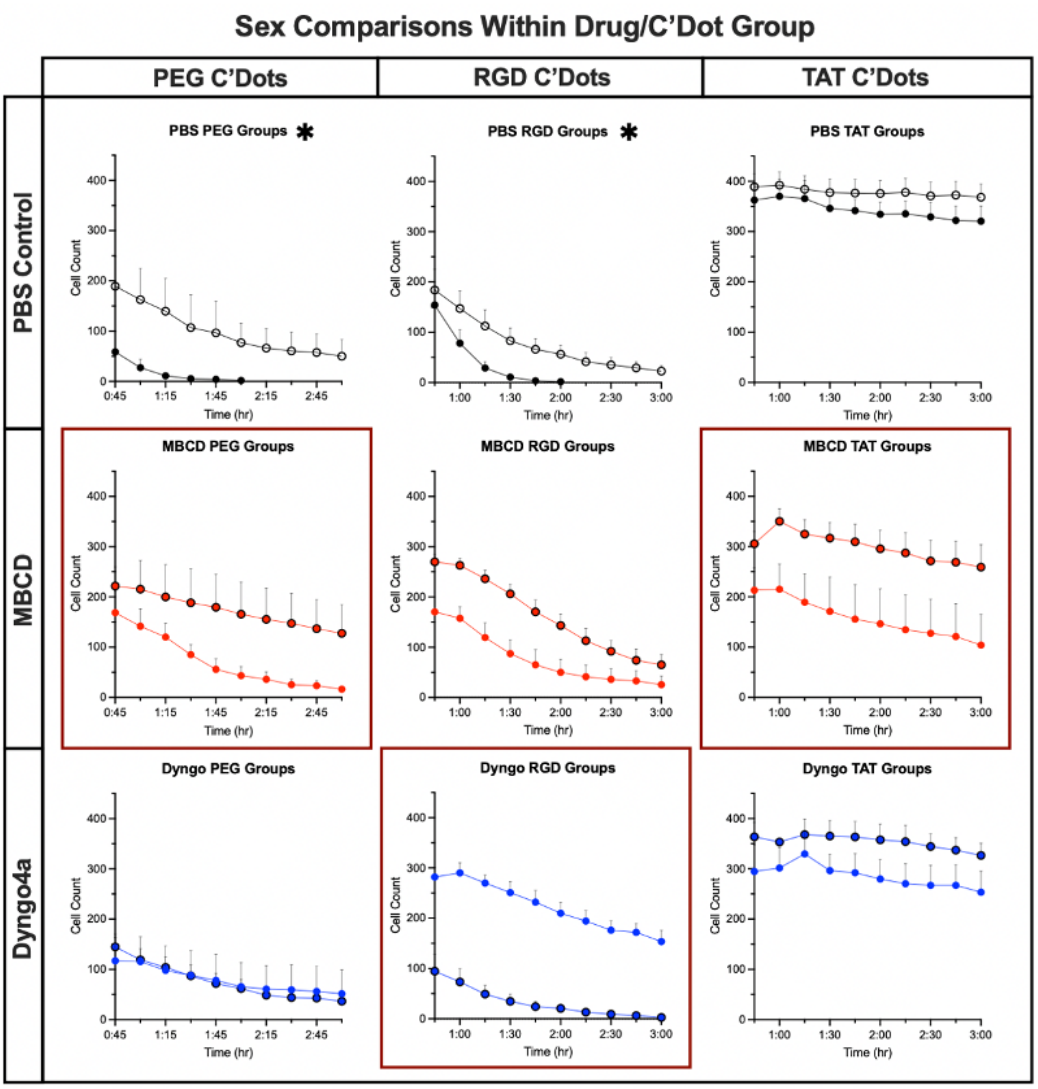

Males

Females

Sex Comparisons	PEG C'Dots	RGD C'Dots	TAT C'Dots
PBS	No Sex Difference	No Sex Difference	No Sex Difference
MBCD	0.026	No Sex Difference	0.016
Dyngo	No Sex Difference	0.0001	No Sex Difference

*Note: Because there are zeros in the data, PBS PEG and RGD differences are likely under-appreciated (Significant in log transformed data) .

Fig. 14. Figure S6: Plots of mixed model comparisons of sex within C'Dot and drug groups for the extended clearance data. Comparisons with significant differences are boxed in red. Asterisks denote that the untransformed data with very low or zero values may be under-appreciated in this mixed model. $P \leq 0.05$, Error = ±SEM.

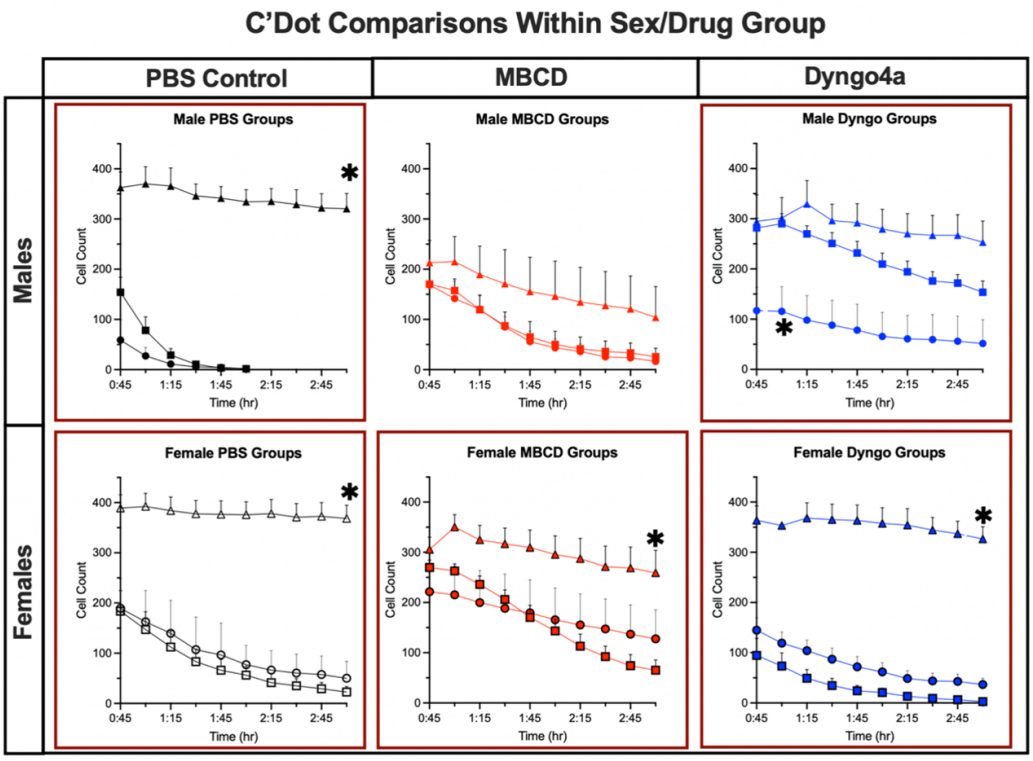

● PEG
■ RGD
▲ TAT

C'Dot Comparisons	PBS	MBCD	Dyngo
Male	PEG-**TAT** <0.0001 RGD-**TAT**<0.0001	No C'Dot Differences	**PEG**-RGD 0.002 **PEG**-TAT 0.0002
Female	PEG-**TAT** <0.0001 RGD-**TAT** <0.0001	PEG-**TAT** 0.021 RGD-**TAT** 0.011	PEG-**TAT** <0.0001 RGD-**TAT** <0.0001

Fig. 15. Figure S7: Plots of mixed model comparisons of C'Dots within drug and sex groups for extended clearance data. Comparisons with significant differences are boxed in red. Asterisks denote the group that is distinct from the others within the plot. $P \leq 0.05$, Error = ±SEM.